Development of Nano-oxide Dispersed Austenitic Stainless Steels by Mechanical Alloying Followed by Conventional Sintering and Spark Plasma Sintering

Sravan Kumar Sambaraj

(Roll No. 613MM3001)

Department of Metallurgical and Materials Engineering
National Institute of Technology, Rourkela
May, 2016

Development of Nano-oxide Dispersed Austenitic Stainless Steels by Mechanical Alloying Followed by Conventional Sintering and Spark Plasma Sintering

A thesis
submitted in partial fulfilment of the requirements for the degree of

Master of Technology (Research)

By

Sravan Kumar Sambaraj

(Roll No. 613MM3001)

Under the supervision of

Dr. Swapan Kumar Karak

Department of Metallurgical and Materials Engineering
National Institute of Technology Rourkela
May, 2016

Department of Metallurgical and Materials Engineering
National Institute of Technology Rourkela

May, 2016

Supervisor's Certificate

This is to certify that the work presented in this dissertation entitled "Development of Nano-oxide Dispersed Austenitic Stainless Steels by Mechanical Alloying Followed by Conventional sintering and Spark plasma sintering" by "*Sravan Kumar Sambaraj*", Roll Number 613MM3001, is a record of original research carried out by him under my supervision and guidance in partial fulfilment of the requirements of the degree of *Master of Technology (Research) in Metallurgical and Materials Engineering*. Neither the thesis nor any part of it has been submitted for any degree or diploma to any institute or university in India or abroad.

Swapan Kumar Karak
(Supervisor)

Dedicated to My Parents
Chandra Shekar and Satya Kumari

Declaration of Originality

I, Sravan Kumar Sambaraj, Roll Number 613MM3001 hereby declare that this thesis entitled “Development of Nano-oxide Dispersed Austenitic Stainless Steels by Mechanical Alloying Followed by Conventional Sintering and Spark Plasma Sintering” represents my original work carried out as a postgraduate student of NIT Rourkela and, to the best of my knowledge, it contains no material previously published or written by another person, nor any material presented for the award of any other degree or diploma of NIT Rourkela or any other institution. Any contribution made to this research by others, with whom I have worked at NIT Rourkela or elsewhere, is explicitly acknowledged in the dissertation. Works of other authors cited in this dissertation have been duly acknowledged under the section "Bibliography". I have also submitted my original research records to the scrutiny committee for evaluation of my dissertation. I am fully aware that in case of any non-compliance detected in future, the Senate of NIT Rourkela may withdraw the degree awarded to me on the basis of the present dissertation.

May, 2016
NIT Rourkela

Sravan Kumar Sambaraj

ACKNOWLEDGEMENTS

I would like to express my sincere appreciation to my Supervisor, Dr. Swapan Kumar Karak, Metallurgical & Materials Engineering Department, National Institute of Technology Rourkela for his constant guidance and encouragement without which this work would not have been possible. I am grateful to his unwavering support and inspiration. I am also thankful to him for giving me sufficient time so I could perform to my best level.

I would also like to extend my sincere gratitude to Prof. S. C. Mishra, Head of the Department, Metallurgical and Materials Engineering, National Institute of Technology Rourkela for his constant guidance and support.

I thank profusely Mr. S.B. Chandrasekhar, Scientist-E, ARCI, Hyderabad for his help in carrying out spark plasma sintering at the centre.

I am also thankful to Mr. S. Pradhan for his technical guidance in conducting scanning electron microscopy.

I am ever thankful to my senior Mr. Mohan Nuthalapati for helping me and providing necessary insight during experimentation. I use this opportunity to express my deep sense of gratitude to my friends and seniors Mr. D. Narsimhachary, Mr. Trinath Talapaneni and Mr. P. Sreekar for their support in my difficult times.

It is my privilege to thank Mr. K Anand Babu, Mr. Muddu Alaparthi, Mr. Rameez Malik, Mr. Subrat Kumar Bhuyan, and Mr. Ashish Giri for their constant encouragement during my research period.

I am forever indebted to my parents who work and live for my well-being.

Sravan Kumar Sambaraj

Abstract

Nano-oxide dispersed austenitic alloys are widely used as structural components in different applications such as heat exchanger parts and pressure vessels in thermal or fusion nuclear power plants. Austenitic stainless steels are the main candidate materials in residual heat removal circuits of pressurised water reactor applications. As nuclear applications require high-temperature strength of the candidate material, improving strength of austenitic stainless steels is a challenge. By dispersing fine oxide particles into austenitic matrix higher strength of the material could be achieved.

The present work aims at synthesis of 70.0Fe-19.0Cr-11.0Ni (alloy A), 69.0Fe-19Cr-11Ni-1.0Y_2O_3 (alloy B), 69.0Fe-19Cr-11Ni-1.0TiO_2 (alloy C) (all in wt %) each synthesized through mechanical alloying and subsequent consolidation by conventional sintering and spark plasma sintering methods. Following this mechano-chemical synthesis and consolidation, extensive effort has been undertaken to characterize the as-milled and consolidated products by X-ray diffraction study, scanning electron microscopy, optical microscopy, energy disperse spectroscopy, followed by evaluation of physical (density and porosity), mechanical (hardness and wear resistance) and chemical (oxidation resistance) properties. The average particle size of alloy A powder decreased from 50.86 ± 6.19 µm to 3.5 ± 1.96 µm with increase in milling time from 0 h to 40 h, and the same phenomenon was observed in mechanical alloying of alloy B and alloy C powders. Samples sintered by spark plasma sintering (SPS) recorded high hardness values (476.0 HV - 724.4 HV) which are nearly 1.5 - 2.0 times the hardness values (268.0 - 464.9 HV) of same alloys consolidated by conventional sintering. Furthermore, wear resistance property of spark plasma sintered alloys, in the range of 3.17×10^{-7} - 15.62×10^{-7} mm^3/mm, followed similar kind of trend as hardness. The wear rate of SPS alloy C (3.17×10^{-7} mm^3/mm) is 1/5th the wear rate of alloy C sintered by conventional sintering (16.8×10^{-7} mm^3/mm). The rate of oxidation of the present austenitic steel decreased with addition of nano-oxides in general and samples sintered by spark plasma sintering show the lowest rate of oxidation. Alloy C sintered by spark plasma sintering offers the maximum improvement in terms of mechanical and oxidation properties as compared to the other alloys and other sintering technique. Thus, it was concluded that mechanical alloying followed by spark plasma sintering (SPS) is the most promising route for synthesizing oxide dispersed austenitic matrix offering attractive mechanical properties.

Keywords: Oxide Dispersion; Austenitic Steel; Mechanical Alloying; Conventional Sintering; Spark Plasma Sintering; Mechanical Properties; Oxidation Study

Contents

Supervisor's Certificate **ii**
Declaration of Originality **iv**
Abstract **vi**
Contents **vii**
List of Figures **ix**
List of Tables **xii**

1 Introduction **1**

1.1 Motivation for the Present Work 1
1.2 Scope and Objectives of the Present Work 2
1.3 Thesis Outline 3

2 Literature Review **4**

2.1 General Background 4
2.2 Austenitic Stainless Steels and Applications 4
2.3 Oxide Dispersion Strengthened (ODS) Steels 6
  2.3.1 Desired Properties and Microstructure of ODS Steels 6
  2.3.2 Oxide Dispersion Strengthened Austenitic Steels 7
2.4 Mechanical Alloying 8
  2.4.1 Genesis 8
  2.4.2 Types of Milling Equipment 8
  2.4.3 Scope and Mechanism of Mechanical Alloying 9
  2.4.4 Significance of Process Parameters on Microstructure Evolution and Properties 12
2.5 Methods for Consolidation of Nano-Structured Powders 15
  2.5.1 Conventional Powder Consolidation 15
  2.5.2 Pressure – Assisted Consolidation Methods 16
  2.5.3 Non- Conventional Consolidation Methods 17
2.6 Densification of Mechanically Alloyed Powders 21
2.7 Strengthening Mechanism in ODS Steels 22
  2.7.1 Matrix Strengthening 22
  2.7.2 Dispersion Strengthening Mechanism 22
2.8 Dislocation - Particle Interaction in ODS Alloys 23
2.9 Oxidation Behaviour of ODS steels 24
2.10 Open Questions and Future Scope of Study 24

3 Experimental Details **26**

3.1 Raw materials and Alloy Selection 27
3.2 Mechanical Alloying (MA) of Austenitic Stainless Steels 27
3.3 Consolidation of Alloy Powders 28
    3.3.1 Conventional Sintering 28
    3.3.2 Spark plasma Sintering 29
3.4 Characterization of Powders and Sintered Products 30
    3.4.1 X-Ray Diffraction 30
    3.4.2 Particle size Analysis of Powders 30
    3.4.3 Optical Microscopy 30
    3.4.4 Scanning Electron Microscopy and Energy Dispersive X-ray Microanalysis 30
    3.4.5 Density and Porosity Measurement 31
    3.4.6 Hardness Measurement 31
    3.4.7 Wear Behavior Study 31
    3.4.8 Oxidation Study 32

4 Results and Discussions **33**

4.1 Synthesis and Characterization of Powders 33
    4.1.1 Phase Evolution during Mechanical Alloying 33
    4.1.2 Morphology and Size of Powder Particles 34
    4.1.3 Crystallite Size and Residual Strain Calculations 36
    4.1.4 Compositional Micro-analysis of Powders by EDS 38
4.2 Characterization and Properties Evaluation of Sintered products 40
    4.2.1 Conventionally Sintered Products 40
    4.2.2 Spark Plasma Sintered Products 42
    4.2.3 Evaluation of Physical and Mechanical Properties of Consolidated Products 47
4.3 Isothermal Oxidation Study of Consolidated Products 53
4.4 Comparison of Properties 58

5 Summary and Conclusion **61**

Future Work **63**
Bibliography **64**
Publications and Conference Presentations **70**
Bio-Data **71**

List of Figures

Figure No.	Figure Description	Page No.
Fig.2.1	Available stainless steel alloy systems	5
Fig.2.2	Steps in mechanical alloying process 1.Initial particles, 2. Flattering, 3. Welding, 4. Fracturing and welding, 5. Final alloy particle	10
Fig.2.3	(a) Four vial planetary ball mill equipment (b) Schematic representation of planetary ball-mill	11
Fig.2.4	Schematic showing fusion and fracturing of powder particles between grinding media in mechanical alloying	11
Fig.2.5	(a) SEM micrograph depicting the convoluted lamellar structure obtained during milling of a ductile-ductile component system (b) Schematics of microstructural evolution during milling of a ductile - brittle combination of powders	12
Fig.2.6	ODS-9Cr steel powder at (a) 1 h, (b) 2 h, (c) 3 h, (d) 4 h of milling	14
Fig.2.7	Single action and double action powder compaction	16
Fig.2.8	Schematic of Spark plasma sintering setup	19
Fig.2.9	Various stages in mechanism of neck formation in SPS process	20
Fig.2.10	Schematic diagram of matter transport paths for two sintering particles	21
Fig.3.1	Flowchart of series of experiments carried out in the present work	26
Fig.3.2	Thermal cycle at 1150 °C temperature during conventional sintering	28
Fig.3.3	Thermal cycle for different temperatures during spark plasma sintering	29
Fig.3.4	Schematic of wear testing equipment	32

Fig.4.1 X-ray diffraction profiles of (a) alloy A, (b) alloy B, (c) alloy C subjected to mechanical alloying for 0 h (manually blended before mechanical alloying) to 40 h 34

Fig.4.2 FE-SEM micrographs of alloy A powder at different milling times. (a) 0h, (b) 5 h, (c) 10 h, (d) 20 h, and (e) 30 h, (f) 40 h 35

Fig.4.3 Variation in crystallite size (nm) and residual strain (%) with increasing milling time (h) of (a) alloy A , (b) alloy B, and (c) alloy C powders 38

Fig.4.4 EDS spectrums of 40 h mechanically alloyed powders of (a) alloy A, (b) alloy B, and (c) alloy C 39

Fig.4.5 X-ray diffraction patterns of conventionally sintered (at 1150 °C) Alloy A, Alloy B and Alloy C 40

Fig.4.6 FE-SEM micrographs of (a) alloy A, (b) alloy B, (c) alloy C conventionally sintered at 1150 °C for 1 h 41

Fig.4.7 EDS patterns of (a) alloy A, (b) alloy B, (c) alloy C processed by conventional sintering 42

Fig.4.8 XRD patterns of samples sintered by spark plasma sintering (SPS) at different temperatures: (a) alloy A, (b) alloy B, and (c) alloy C 43

Fig.4.9 Scanning electron micrographs (FE-SEM) of alloy A processed by spark plasma sintering at (a) 800 °C, (b) 900 °C, (c) 1000 °C 44

Fig.4.10 Scanning electron micrographs (FE-SEM) of alloy B processed by spark plasma sintering at (a) 800 ºC, (b) 900 ºC, (c) 1000 ºC 45

Fig.4.11 Scanning electron micrographs (FE-SEM) of alloy C processed by spark plasma sintering at (a) 800 °C, (b) 900 °C, (c) 1000 °C 46

Fig.4.12 EDS spectrums of (a) bright phase and (b) dark phase in spark plasma sintered alloy A 46

Fig.4.13 Variation of density and porosity values of (a) alloy A, alloy B and alloy C processed by conventional sintering at 1150^{o}C, (b) alloys processed by spark plasma sintering at 800 °C, 900 °C, 1000 °C 48

Fig.4.14 Vickers hardness values of all alloys processed by conventional sintering and spark plasma sintering (SPS) 49

Fig.4.15 Wear rate values of all alloys processed by conventional sintering and spark plasma sintering 50

Fig.4.16 Optical microscope images showing wear tracks of (a) alloy A and (b) alloy B spark plasma sintered at 800 °C 52

Fig.4.17 Optical microscope images showing wear tracks of (a) alloy B and (b) alloy C spark plasma sintered at 900 °C 52

Fig.4.18 Optical microscope image showing wear track of alloy C spark plasma sintered at 1000 °C 52

Fig.4.19 Kinetics of isothermal oxidation of SPS alloy A, alloy B and alloy C (sintered at 900 °C) and conventionally sintered alloy A, alloy B and alloy C in terms of mass gain per unit area as a function of time during isothermal exposure to 1000 °C in dry air 53

Fig.4.20 Rate constant during isothermal exposure to 1000 °C dry air for alloy A, alloy B and alloy C consolidated by two different processes namely; conventional sintering at 1150 °C and spark plasma sintering at 900 °C 54

Fig.4.21 SEM micrographs of conventionally sintered (a) alloy A, (b) alloy B, and (c) alloy C, and spark plasma sintered (d) alloy A, and (e) alloy B and (f) alloy C after isothermal oxidation at 1000 °C for 50 h 55

Fig.4.22 X-ray diffraction patterns of conventionally sintered and oxidised (a) alloy A, (b) alloy B, and (c) alloy C after isothermal oxidation at 1000 °C for 50 h 57

Fig.4.23 Fig.4.23: X-ray diffraction patterns of SPS (a) alloy A, (b) alloy B, and (c) alloy C after isothermal oxidation at 1000 °C for 50 h 58

List of Tables

Table No.	Table Description	Page No
Table 3.1	Details of austenitic stainless steel and nano-oxide powders used for producing desired alloys	27
Table 3.2	Chemical compositions of Individual Alloys in wt. %	27
Table 3.3	Specifications of the spark plasma sintering unit	29
Table 4.1	Average particle size of milled powder (Alloy A) at different milling times	36
Table 4.2	Crystallite Size (nm) and Residual strain (%) values at different milling times (h)	37
Table 4.3	Summary of EDS analysis of 40 h mechanically alloyed powders	39
Table 4.4	Summary of EDS analysis of bright phase and dark phase in alloy A	42
Table 4.5	Summary of EDS analysis of bright phase and dark phase in SPS alloy A	47
Table 4.6	Density and porosity values of conventional and spark plasma sintered alloys	48
Table 4.7	Summary of physical and mechanical properties of all alloys developed by conventional and spark plasma sintering	58

Chapter 1

Introduction

1.1 Motivation for Present Work

Ever increasing technological needs of the world necessitate suitable materials to be used. Materials scientists have thus continuously aimed at improving properties and performance of materials and also design new ones for specific applications termed as advanced materials. Developing advanced materials primarily involves fixing a certain chemical composition and developing techniques to economically produce in a mass scale. In order to fulfil these objectives, new elements were added to base materials and hence harnessing properties of each element. This came as a challenge as addition of alloying elements to base materials and thus producing an advanced alloy involved systematic synthesis and control of structure on which depends the desired properties. Synthesis of advanced alloys by conventional melting and casting route is very difficult because, the density differences between various alloying elements and base materials result in inhomogeneous structure. To have better control of structure and obtain optimised properties non-equilibrium processing techniques have been employed. Non-equilibrium processing techniques which have gained scientists interest are rapid solidification from the liquid state, plasma processing, mechanical alloying, and vapour deposition. Scientific investigations have proven that non-equilibrium processing techniques resulted in structural homogeneity and improved mechanical properties [1]. The effectiveness of these individual processes can be determined by comparing the energy in the processes which deviates from equilibrium. Mechanical alloying deviates more from equilibrium than rapid solidification. Also, the mechanical alloying technique is relatively simple and inexpensive and thus used widely [2].

Mechanical alloying is essentially a powder processing technique, also termed as mechanical milling, wherein the powder particles are subjected to repeated cold welding, fracturing, and rewelding in a ball mill. The mechanical energy in this process transfers to the particles and induces strain in them consequently refinement of particles occurs. When different alloying elements are blended in powder form by mechanical alloying process, the resultant products would be metastable phases such as intermetallics, nano-structured phases, and high energy mixing compounds, metallic glasses and supersaturated solid solutions. The development of mechanical alloying was an industrial necessity during 1960s in order to produce nickel-base superalloys with oxide dispersions which improved high temperature strength [3]. Recently more emphasis is being laid on oxide dispersion strengthened steels as these are candidate materials for GEN IV fission reactors and fusion reactors for example Demonstration Power plant (DEMO). Conventional low activation Fe-Cr steels have poor creep properties above 550 °C but the oxide dispersion strengthened variety of the same steels exhibit excellent high temperature properties. Also, these steels retain mechanical strength and resistance to corrosion/oxidation at elevated temperatures [4,5].

Other fabrication routes namely EDTA–citrate complex method and sol–gel method have been reported to produce oxide dispersion strengthened steels [6]. However, mechanical alloying process has been proven to be most effective alloying technique and is being widely used. Various categories of advanced steels are oxide dispersion strengthened (ODS) ferritic steels, ODS ferritic-martensitic steels and ODS austenitic steels. Out of all these materials the most oxidation and corrosion resistant steels are austenitic steels. They are also not extensively studied compared to ferritic and ferritic- martensitic steels. Austenitic stainless steel grades such as 304, 304L, 316 are potential candidate materials for future advanced nuclear reactors which operate at >550 °C. Hence, it is of very high importance to produce these steels with enhanced high temperature properties.

1.2 Scope and Objectives of the Present Work

(1) Synthesis of three different austenitic alloys with nominal compositions of 70Fe-19Cr-11Ni (alloy A), 69Fe-19Cr-11Ni-1.0Y_2O_3 (alloy B) and 69Fe-19Cr-11Ni-1.0TiO_2 (alloy C) (all in wt. %) by mechanical alloying for 40 h and two different sintering processes i.e. conventional sintering and spark plasma sintering. Conventional sintering of all alloys at 1150 °C for 1 hour and spark plasma sintering at 800, 900, and 1000 °C with 5 minutes holding time, 200 °C/min heating rate which would be same for all alloys.

(2) Study of particle size of mechanical alloyed powder samples at different stages of milling (0 h, 5 h, 10 h, 20 h, 30 h and 40 h) through particle size analysis and micro structure analysis (SEM).

(3) Study of phase evolution, microstructural evolution and chemical composition analysis in mechanical milled powder samples and sintered pellets through X-ray diffraction analysis (XRD), scanning electron microscopy (SEM) and electron dispersive spectroscopy (EDS) respectively.

(4) Evaluation and comparison of physical property (density) and mechanical properties (hardness and wear resistance) of the three different alloys consolidated at different sintering temperatures and by different sintering techniques.

(5) To study oxidation behaviour of both conventional and spark plasma sintered alloys when subjected to 1000 °C temperature for 50 h.

1.3 Thesis Outline

The thesis is presented in five chapters. **Chapter 1** contains the general background as well as the challenges and motivation to pursue the present work. The discussion includes an overview of the objectives and scope of the present investigation. **Chapter 2** gives extensive review of available literature relating to materials and methods used in the present work. The examples and research findings that have been mentioned in this chapter are duly referred wherever necessary. **Chapter 3** meticulously provides information regarding all kinds of experimentations carried out in this research. Which includes, (i) synthesis of all the three alloys with 1.0 wt.% nano-Y_2O_3/TiO_2 dispersion, consolidation by conventional sintering and spark plasma sintering (SPS) and (ii) characterization of microstructure, phase aggregate, physical/mechanical/Chemical properties of interest. **Chapter 4** deals with the results and discussions on phase transformation, crystallite size reduction and microstructural evolution during mechanical alloying. Also, the effect of milling time has been discussed. Furthermore, this chapter includes discussion on the evaluation and comparison of physical (density, porosity), mechanical (hardness and wear resistance) and oxidation resistance properties of the three different alloys developed by different processing methods with the relevant results reported in the literature. The thesis conclusions drawn from the analysis of experimental outputs are listed in **Chapter 5.**

The references cited within each chapter are listed at the end of the thesis. In addition, the figures and tables are numbered independently in each chapter.

.

Chapter 2

Literature Review

2.1 General Background

Stainless steels are one of the most important categories of alloys as they possess desired properties for a wide variety of applications. The applications that depend on the use of stainless steels range from low-end, i.e. furniture and cooking utensils, to very advanced applications such as space vehicles making the use of stainless steels quite essential. The amount of chromium, of at least about 11% by weight, present in stainless steels is directly responsible for their “stainlessness” nature. At this amount of chromium, an adherent chromium oxide forms on the surface of steel. In addition to chromium other alloying elements are added to enhance properties and to stabilise certain phases. For example Nickel is added to stabilise austenite phase at room temperature [7]. Hence by rightly varying the steel chemical composition different microstructures namely Austenitic, Ferritic and Martensitic may be obtained in the steel. Based on these three important microstructures the stainless steels are classified into austenitic stainless steels, ferritic stainless steels, martensitic stainless steels, duplex stainless steels, Mn-N substituted austenitic stainless steels and precipitation hardening stainless steels. For convenience the development of additional PM grades of stainless steel will adhere to these categories. Stainless steels which are fully austenitic are non-magnetic but those containing fully martensitic or fully ferritic microstructures possess ferromagnetism [8].

2.2 Austenitic Stainless Steels and Applications

Austenitic stainless steels are the most common and known categories of stainless steels. These steels are non-magnetic in nature and contain Chromium (Cr) in the rage of 16 - 25% and nitrogen in solid solution which are responsible for their high corrosion resistance. Some of the austenitic stainless steels can resist boiling sea water. They possess high degree of toughness and are highly weldable and formable. Austenitic stainless steels in wrought form are used for a wide range of applications more so than

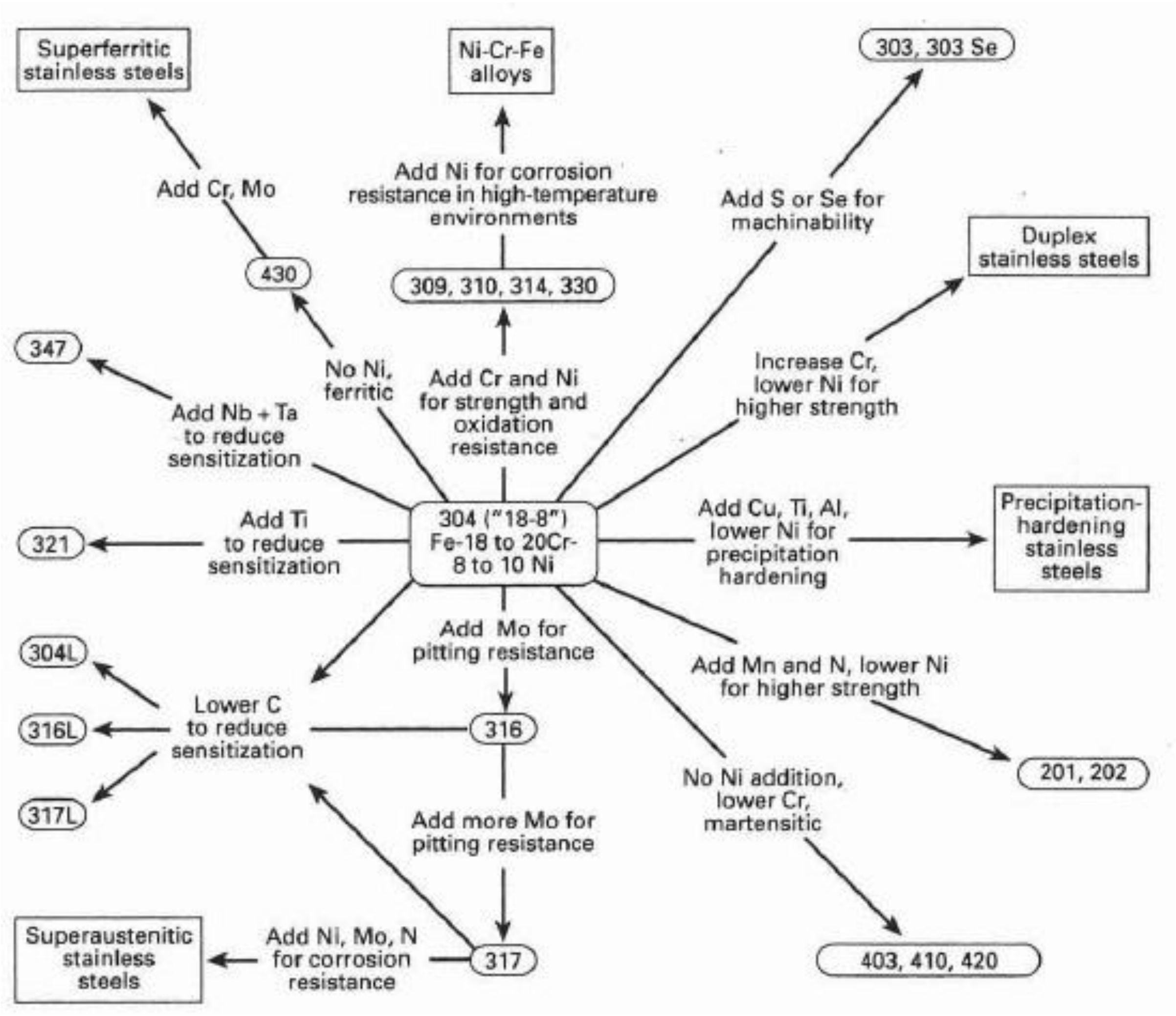

Fig.2.1: Available stainless steel alloy systems [8].

other types of stainless steel because of their excellent formability, weldability and corrosion resistance. They can be used as materials for operations involving low (cryogenic) temperatures and high temperature applications such as furnaces, jet engines and also nuclear reactors as these steels have good creep resistance to higher temperatures. Few drawbacks of these steels are they are relatively less resistant to cyclic oxidation than ferritic steel, susceptibility to stress corrosion cracking and thermal fatigue. Because of their greater thermal expansion co-efficient, break down of protective oxide layer takes place resulting in low cyclic oxidation resistance. Metal powder Industries Federation standard 35 lists the most common austenitic grades of stainless steel used by PM manufacturers. These steels include 303L, 304L, and 306L. All stainless steel grades manufactured by conventional press and sinter powder metallurgy are shown in Fig.2.1. Among austenitic grades AISI 304 stainless steel is one of the widely investigated material because of its very good corrosion resistance, particularly in sulfidizing and oxidizing atmospheres and in molten salts [9]. AISI 304L stainless steel is commonly used in the manufacture of larger vessel internals in pressurized water reactor (PWR) and pressurized heavy water reactor (PHWR) environment. Manuela Fulger et al [10] studied the effect of oxide layers on corrosion resistance of AISI 304L stainless steel and compared the general corrosion behaviour of this steel in SCW at temperature from 723 K to 873 K under 25 MPa pressure. It was found that the oxidation of AISI 304L stainless steel between these temperatures, follows parabolic rate. This behaviour indicates that it is driven by diffusion process and the steel is self-protecting. These stainless steels processed by using powder metallurgy techniques do not have corrosion resistance on par with the wrought form of same alloy. The reason being presence of porosity in the powder metallurgy processed steels and impurities picked during processing [11]. Many studies have been carried out to improve the overall properties of PM processed austenitic stainless steels as their mechanical properties for nuclear reactor application are inadequate. Variety of these attempts include employing alternate sintering techniques like hot-pressing, hot-isostatic pressing, non-conventional consolidation methods such as microwave sintering [12], pulse plasma sintering [13], and spark plasma sintering [14]. Also, researchers considered addition of alloying elements such as Nb, W, Ti and nano-oxides such as Y_2O_3, TiO_2 etc. into the steel matrix through mechanical alloying process. Particularly, more importance was given to addition of nano-oxides because ODS (oxide dispersion strengthened) steels have potential to suppress void formation due to slow recovery of initial dislocation structure immobilized by oxide particles. Further changing the ODS steel chemical composition researchers have added elements like Ti, Zr, W and Hf. The following sections discuss about ODS steels and ODS austenitic steels.

2.3 Oxide Dispersion Strengthened (ODS) Steels

2.3.1 Desired Properties and Microstructure of ODS Steels

Oxide dispersion strengthened (ODS) steels are basically being developed to meet the applications involving high temperatures in nuclear reactors. Conventional ferritic/martensitic steels have desired properties but upper operating temperature of these steels limits to 550-600 °C and in the case of conventional austenitic steels the high temperature strength needs to be improved. For the purpose of improving this limit to higher temperatures and retain the properties inherent in the base alloy (like high thermal conductivity, low thermal expansion coefficient, and low void swelling, high temperature strength etc.) oxide particles are added to the base alloy, primarily through mechanical alloying. This high density of small oxide particles distributed though out the steel matrix is responsible for the elevated temperature strength [15]. Also, the oxide particles in the steel matrix act as sinks for defects like helium bubbles and the nucleation of large voids is delayed. Other detrimental effects at high temperatures such as fatigue, grain boundary sliding can be prevented by dispersion of ultra fine oxides [4, 16]. Hence the oxide particles structure is very crucial for desired properties. The microstructure should consist of homogeneously distributed oxide particles in the steel matrix. Apart from oxide particles added to the steel, nanoscaled second phases formed from interaction of oxides and added metals, during MA process, directly influence the strengthening. A bimodal nano-sized grain structure with improved ductility was obtained by introducing copper to ODS ferritic steel [17]. The experiment by R. Kasada et al [18], in which aluminium is added along with oxide dispersions resulted in formation of coarse Y-Al oxides and hence has reduced the effect of strengthening. Another variant of ODS ferritic steels are nanostructured ferritic steels (NFSs), which possess further enhanced properties such as excellent creep strength and significant radiation resistance [19]. M.J. Alinger et al [20] found that nanostructured ferritic steel (NFS) produced by mechanical alloying of ferritic steel with Ti and Y_2O_3 contain Y-Ti-O enriched nanoclusters with merely 1-2 nm diameter. Mechanical alloying dissolves yttrium (Y) and oxygen (O) in base alloy matrix. In the presence of Ti the dissolved Y and O precipitate as nanoclusters (NCs) and oxides after hot consolidation. Enhanced properties of the steel have been attributed to these nanoclusters (NCs).

2.3.2 Oxide Dispersion Strengthened Austenitic Steels

Although ODS ferritic steels have been developed, these steels have poorer corrosion resistance compared to austenitic steels [21]. Austenitic stainless steels are considered for this purpose because of their superior overall mechanical properties and comparatively very good oxidation and corrosion resistance than ferritic – martensitic steels. But the major challenge pertaining to application of austenitic stainless steels is to improve high temperature creep strength and ultimate tensile strength (UTS) [22]. Research interest has been more on 316 and 304 austenitic stainless steel with alloying additions in minor quantity, such as Ti, Mo, W, and Y_2O_3 dispersions. Zhangjian Zhou et al [22] have extensively characterised the morphology and properties of a 304 ODS austenitic stainless steel and found that the most of the dispersoids are complex oxides of around 20 nm size. The ODS austenitic steel has very high tensile strength and good ductility at room and high temperatures. It has been observed that Y_2O_3 dissolves in the steel matrix during milling and the alloying elements get into solid solution. It has also been reported that very small quantity of oxide dispersions can accelerate the solid-solution formation and also these particles retard the grain growth during consolidation. Forging of these sintered

ODS steel has resulted in decreased porosity and hence improving uniformity in microstructure and ductility while retaining the same ultimate tensile strength [23, 24].

2.4 Mechanical Alloying

2.4.1 Genesis

Non-equilibrium processing techniques are promising in order to produce better materials with improved/desired properties when compared to materials produced by conventional techniques. Mechanical alloying is a solid state synthesis process that consists of repeated cold-welding, fracturing, dynamic recrystallization and mechanically activated inter-diffusion among the powder particles in a high energy ball mill [25]. MA is an established technique to produce oxide dispersion strengthened (ODS) nickel-Iron-based materials. Metastable phases and equilibrium phases can also be synthesized by mechanical alloying. Although this technique was developed, by Benjamin in 1966, to develop oxide dispersion strengthened nickel base superalloy for gas turbine applications, different materials are being produced which find applications such as hydrogen storage materials, gas absorbers, heaters, fertilizers, cosmetics, catalysts and waste management. However, even though the history of mechanical alloying processing technique for industrial applications is decades long, the basic understanding of mechanism of MA has been achieved only recently.

2.4.2 Types of Milling Equipment

Various types of mills are being used to produce mechanically alloyed powders; they are as follows SPEX shaker mills, planetary ball mills, Attritor mills, Commercial mills. SPEX mills are high energy variety of mills manufactured by SPEX CertPrep Metuchen, NT. The typical SPEX mill consists of a vial in which sample and grinding balls are placed. The vial swings to and fro thousand times in a minute. The movement of the clamp is as fast as about 1200 RPM which results in high ball velocities and subsequently ball impact is very high [2]. A number of vial materials are used in SPEX materials such as tungsten carbide, hardened steel, zirconia, alumina stainless steel, silicon nitride, methacrylate and plastic. Relatively simple equipment for efficient grinding of materials is a planetary ball mill. It consists of two or more vials (which rotate around their own axis) installed on a disc which rotates at a given rotations per minute (RPM) which can be preset. In the vial milling media such as chrome steel balls, hardened steel balls, ceramics and also rubber are responsible for effective grinding. Parameters such as physical properties and geometry of these grinding media affect the overall comminution process, the particle sizes after milling and their defects [26]. These parameters are namely: Density of the grinding medium- large size (high density) of grinding medium will transfer higher impact energy to the powder particles. Size of the balls affects the final formation of the powder. It was reported that milling conditions such as small ball sizes, lower ball-to-powder ratio (BPR) and lower energies result in amorphous phases. Small balls develop acute frictional forces which boosts the formation of amorphous phase [27]. High energy planetary ball milling has been hence used to produce ultrafine particles and also amorphous phases. In the recent years it was also demonstrated by using high energy planetary ball milling there is possibility of mechanical coating (MC) on metal substrates can be done [28]. In the case of ceramic powders, to produce nano-sized powders particles from coarse particles of micrometer sizes high speed planetary ball milling is advantageous [29]. Another type of milling equipment is attritor mill which essentially generate high energies. In these mills large quantities of powder can be milled (up to 40 kg) at a time, the stirring action of an agitator that has a vertical rotating shaft with horizontal arms. This creates movement between balls, the grinding medium, and the materials being milling. The impact and shear forces are responsible for milling. The grinding medium moves in trajectory motion and collide with powder thereby breaking down particles into smaller sizes [30].

2.4.3 Scope and Mechanism of Mechanical Alloying

It has been repeatedly proven that reduction of particle size can substantially improve properties of the alloy. By using simple equipment i.e. a planetary ball mill, powders of few microns size can be brought to nano sized level, hence a nano- structured alloy is produced [31]. A four vial planetary ball mill equipment and schematic representation of planetary ball-mill are shown in Fig.2.3. In addition to the structure refinement of powder particles, mechanical alloying has few characteristic benefits such as: dissimilar metal elements can be alloyed at room temperature by high energy mechanical milling and the initial nano-sized oxide particles get further refined and as a result ultra fine complex oxide particles are formed [22]. The steps involved in mechanical alloying of dissimilar metal elements are shown in Fig.2.2. Enhanced physical and mechanical properties of nano-structured materials, compared to materials with grain size greater than 1 µm, can be attributed to concentration of large fraction of atoms in the grain boundaries due to very small size (typically 1-100 nm) of the grains [32]. Formation of inter metallic compounds by mechanical milling of elemental powders has not only confirmed that MA is a non-equilibrium processing technique but also led to quite a number of research activities which involved synthesis of different alloy phases such as supersaturated and equilibrium solid solutions, crystalline and quasi crystalline, intermediate phases and amorphous alloys

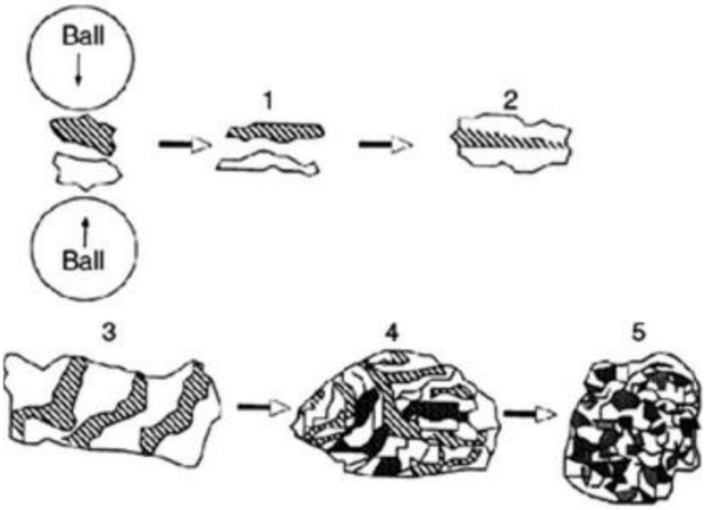

Fig.2.2: Steps in mechanical alloying process 1.Initial particles, 2. Flattering, 3. Welding, 4. Fracturing and welding, 5. Final alloy particle [69].

Hence, it was evident that mechanical alloying offers unique advantages over conventional and other non-equilibrium processing techniques. These advantages are: Novel alloys can be synthesized: elements which are immiscible can be alloyed as MA is completely a solid-state processing technique. Fine dispersion of second phase particles can be produced. It is possible to refine grain sizes to nano scale range. Increase in solid solubility limits of alloying elements. During MA, chemical reactions take place at room temperature, also amorphous phases, disordered structures of ordered intermetallics can be obtained [33-35]. Fig.2.4 shows fusion and fracturing of powder particles between grinding media (balls) in mechanical alloying. The mechanism of mechanical alloying depends upon on the nature of materials being alloyed. It differs for ductile-ductile components, ductile –brittle components and brittle-brittle components. C. Suryanarayana et al [2] states that ductile-ductile combination is best for effective mechanical alloying. In this combination initial stage involves micro forging of powder particles which leads to flat shaped particles. Particles get cold welded and form lamellar structure, Fig.2.5a, with greater work hardening and thereby increase in hardness and brittleness upon further milling.

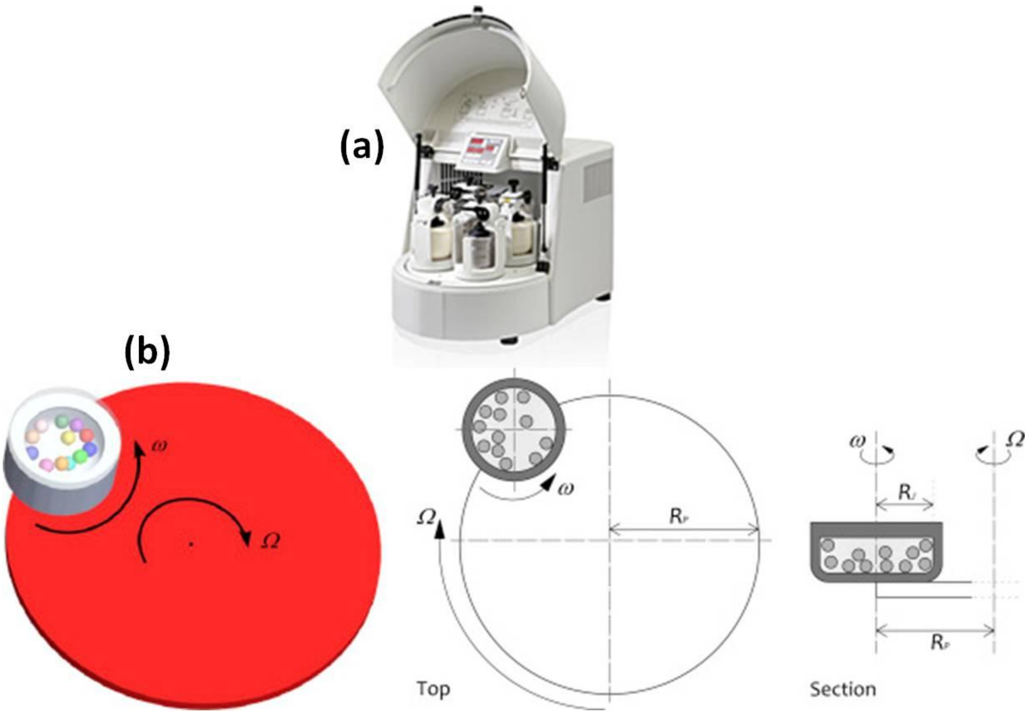

Fig.2.3: (a) Four vial planetary ball mill equipment (b) Schematic representation of planetary ball-mill [26].

As milling is continued the diffusion distance decreases, lattice defect density increases and these combined with heat generated during milling, alloying occurs. At the alloying stage there will be no change in hardness and particle size and hence called steady- state stage.

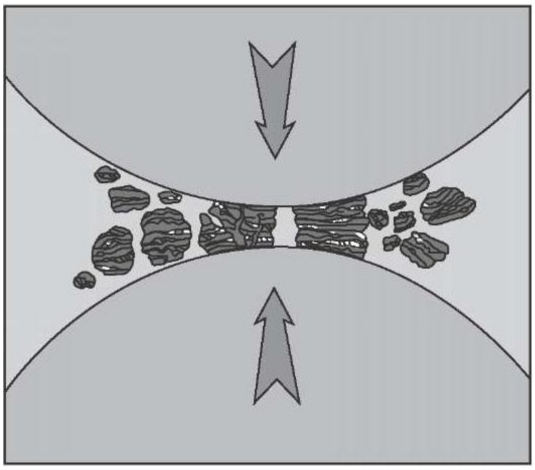

Fig.2.4: Schematic showing fusion and fracturing of powder particles between grinding media in mechanical alloying [70].

J. S. Benjamin et al [36] reports that while mechanical alloying of Cr and Fe powder steady state distribution of powder particle sizes was achieved after more than 100 minutes of milling. Oxide dispersion strengthened alloys come under the category of ductile-brittle combination and during MA of these systems. In general, the mechanism involves flattening of ductile powder particles and fragmentation of brittle particles in the initial stages of milling. On further milling, brittle particles get trapped in the lamellar structured ductile particles and are uniformly dispersed in the ductile matrix [37].

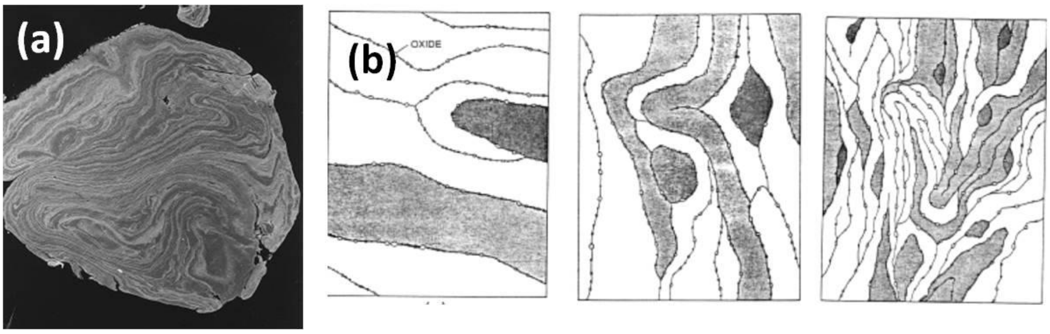

Fig.2.5: (a) SEM micrograph depicting the convoluted lamellar structure obtained during milling of a ductile-ductile component system.(b) Schematics of microstructural evolution during milling of a ductile-brittle combination of powders [2].

The brittle - brittle combination of mechanical alloying has been found difficult to describe. Mechanisms such as surface melting, temperature enhanced deformation; microdeformation and temperature enhanced diffusion have been proposed. It was described that there is deviation from particle morphologies and the usual lamellar structure formed for ductile components. As mentioned earlier the lamellar structure is developed by compressive forces experienced by the powder particles during mechanical alloying. However mechanical alloying of brittle components like Si-Ge has shown that complex stress-states in the compressed particles may lead to neck formation. These stress states can be hydrostatic stress or hydrostatic – tensile stress. Other research findings suggested that the stored elastic stress in the contact region between spherical particles could result in the formation of neck.

2.4.4 Significance of Process Parameters on Microstructure Evolution and Properties

Various process parameters in mechanical alloying include milling temperature, milling time, ball-to-powder weight ratio, process control agent, quantity ratio of powders to be milled and grinding medium size. Reports suggest low milling temperatures take much shorter durations to synthesize metals such as titanium when compared to milling conducted at room temperatures. In the mechanical alloying process with increase in milling time the particle size gradually reduces and residual strain, dislocations in powder crystals increase. In comparison between stearic acid and ethyl alcohol as process control agents (PCA), stearic acid yielded finer crystallite size with spherical powder particles uniformly distributed. After 5 h milling of Fe-Cr-Al alloy in the absence of PCA large particles were observed, which suggest that for true alloying to occur a PCA is necessary. Else excessive cold-welding and associated agglomeration hinder alloying process. Use of stearic acid distributed particles more homogenously and with no agglomeration and decreased particle size. Spherical particles and a little agglomeration occurred when ethyl alcohol was used. It was also reported that large amounts of ethyl alcohol lead to lamellar shape morphology. Stearic acid was found to reduce crystallite size more effectively than ethyl alcohol [38]. Apart from these parameters the milling time within which powder particles size gets reduced is very important, Hiroshi oka et al [21] studied the effect of milling time on PNC316 powder. The alloy powder contained 0.35wt. % Y_2O_3 and X-ray diffraction patterns show disappearance of Y_2O_3 peak after 6 h of milling which was present even after 3 h of milling. The reason for this was mentioned to be reduced Y_2O_3 particle size and or dissolution of Y and O atoms in matrix. Another similar study on microstructural changes while mechanical milling W and W-Y powders was reported by Mingyue Zhao et al [39]. As milling time increased W powders were characterized by refinement in particle size while coarsening occurred in W-Y powders. Since W is brittle in nature the powder particles were first flattened with an oriented morphology. Upon further milling, particles with sizes less than 1 µm became more equiaxed and reached a steady state. In W–Y system powders, they behaved as brittle/ductile powder systems. During the milling process, ductile Y particles acted as a coherent agent that could improve the capacity of cold welding of refined tungsten powders. Therefore, the W–Y powders exhibited spherical-like morphology. While mechanical milling of ODS ferritic steels like 9-Cr powder the particle size first increased after 1 h of milling and then gradually decreased. The spherical shape of powders was turned to disc shape milling. Fig.2.6 shows the morphology ODS-9Cr steel powder at different milling times [40].

The ball-to-powder weight ratio has a significant influence on rate of crystallite size reduction. Although 20:1 ball-to-powder (BPR) weight ratio is recommended, 10:1 ball-to-powder weight ratio (BPR) is most commonly taken one. Generally the effect of ball-to-powder weight ratio is regarded as follows: there should be high degree of movement of balls in the ball mill vials i.e. for the velocity of the balls to be high the amount of powder in the vials should be low relatively to the number of balls. This results in more number of collisions between the grinding media, balls, and the powder. Hence, ball-to-powder weight ratio should be high enough for effective milling process [41]. However, it can be understood from recent publications that ball-to-powder weight ratio alone cannot be used as single most parameter for determining milled powder properties.

Investigations on effect of ball size during milling of aluminium powder by S. Razavi-Tousi et al [42] revealed that when large size balls are used steady state milling time reduced. Large sized balls provide high energy impacts and this is preferred over high number of low energy as in latter case significant part o that energy can be of no use as the impacts do not reach a threshold level to deform powder particles. However microstructural evolution was found to be similar with small and large sized balls but only milling progress varied. In addition to this when different BPRs i.e. 10:1, 20:1 and 30:1 were used to synthesis an Fe-Cr-Al powder, higher BPR resulted in greater level of contamination hence lower level of BPR was recommended [38]. Properties of alloys produced by mechanical alloying and sintering depend upon as milled microstructure, which in turn depends on milling parameters, and sintering process. For example, when alloyed with $Y_2O_3$with increasing milling time Y and O distribute uniformly in the base matrix and also grain refinement takes place resulting in better hardness. The bending strength of the consolidated W–Y compacts was reported to depend on dispersion of Y particles [39].

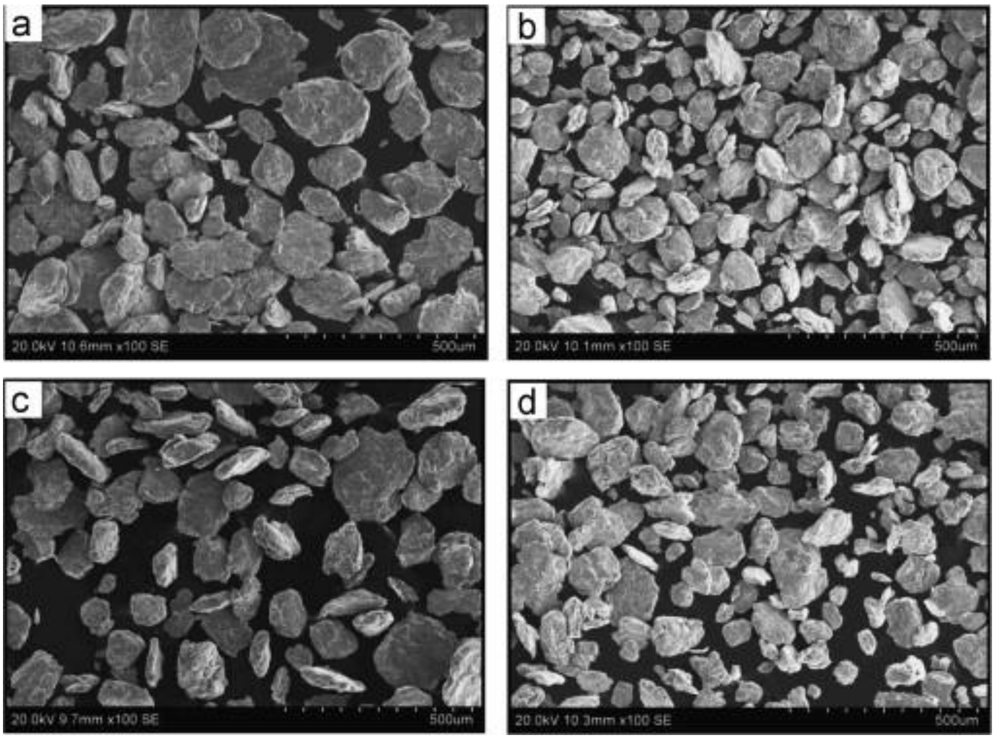

Fig.2.6: Morphology ODS-9Cr steel powder at (a) 1 h, (b) 2 h, (c) 3 h, (d) 4 h of milling [40].

Sintering and subsequent heat treatment has substantial affect on end properties of consolidated products. In ODS steels the oxide particles precipitate in recystallized grains when subjected to annealing after sintering. If fine grain size obtained from mechanical milling could be retained after sintering, the sintered alloys would possess excellent mechanical properties. To achieve this, few non-conventional consolidation techniques are being used, which are discussed in section 2.5.3.

2.5 Methods for Consolidation of Nano-Structured Powders

Sintering is a powder consolidation process and its origin dates back to 6000 BC. The earliest example of sintering is heating of clay objects in an open pit fire to make bricks. In the years 1920 to 1950 it was discovered that consolidation occurs by mass transport mechanism [43]. To understand the process better several investigations have been carried out. Main objective of these investigations was to increase the mass transport and sinter refractory materials or to consolidate at lower temperatures. One such method of activating sintering process involves the use of electric current and was named "spark sintering" and later developed as spark plasma sintering technique [44, 45]. In recent years materials scientists have been using the spark plasma sintering to consolidate nano-structured powders as the end product also retains nano-structure with very less grain growth and retaining properties of powders. The details including construction of sintering equipment and mechanism of different sintering processes, both basic and advanced are as follows:

2.5.1 Conventional Powder Consolidation

Conventional powder consolidation of two aspects i.e. powder compaction and furnace sintering. Compaction is essential to pack the powder particles into a desired shape. In the compaction process the shape and final dimensions are set considering future changes which the powder could undergo during subsequent sintering. One of the main purposes of compaction is to impart sufficient strength which is required for posterior processing. Powder compaction can be carried out both at room temperature or at high temperature. The advantage of high temperature compaction being, the flow behavior of powders is better than in that of room temperature hence resulting in greater green compact density. A typical compaction press consists of fixed die, upper punch and lower punch as shown in Fig.2.7. Different compaction techniques are used which can be distinguished by the relative movement of these three parts of the press.

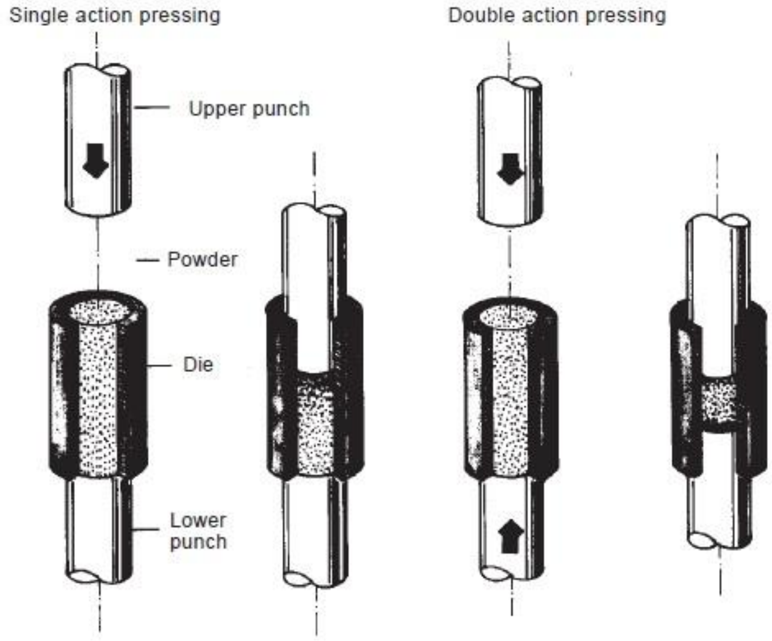

Fig.2.7: Single action and double action powder compaction [71].

In general, dies are fixed and upper punch or/and lower punch are movable. If only one punch is movable it is called single action pressing. While if both the punches are movable the process is called double action pressing. Double action pressing is advantageous over single action pressing due to the fact that in the former process both upper punch and lower punch are movable, dies will be stationary, and the pressure distribution in powder is uniform. But in single action pressing lower punch and die are fixed and only upper punch is movable resulting in high pressure at top and low pressure at bottom. Next stage in consolidation is sintering generally carried out in a furnace at certain fixed temperature and holding time. Mechanisms such as mass transport and pore closure take place and a dense product of desired shape is obtained.

2.5.2 Pressure – Assisted Consolidation Methods

Advanced materials that are being produced possess unusual properties compared to that of materials produced by conventional methods. In general most of these materials are produced using powder metallurgy techniques and these powders attribute their exceptional properties to a metastable condition like nanocrystalline, amorphous or non-equilibrium phase structures. It is definitely a challenge to consolidate such type of powders since under exposure to high temperatures phase transformation occurs. In recent years nano powder densification was done using all pressure-assisted consolidation methods: hot-pressing, HIP, and Ultra-High pressure sintering, pulse plasma sintering, and hydrostatic extrusion. Out of which Hot-pressing and Hot-Isostatic Pressing are widely used:

Hot-Pressing: Hot pressing has typical advantages over pressure-less sintering in obtaining full density products with minimal grain growth. This has been proven by processing nanocrystalline Fe-(9Fe, Mo)$_6$C, ZrO_2-Al_2O_3, and TiO_2. Near net densities, grin sizes less than 100 nm were achieved by mechanical alloying and hot-pressing at 550 °C of Fe-10%Al, Al-10%Ti, and Fe-2% Al.

Hot-Isostatic Pressing (HIP): Hot-Isostatic pressing is a commercial consolidation technique to produce dense products of tool steels, ceramics, Titanium alloys, superalloys. In this method powder is packed into an evacuated sheet metal perform and then simultaneously heated with high pressure in an inert gas pressure vessel. Cheng Hao et al [46] have investigated the application of Hot-isostatic pressing (HIP) treatment in order to improve fatigue properties of the LMD AerMet100steel. It was observed that when LMD steel was HIP treated above austenitization temperature columnar grains if the steel have transformed to equiaxed grains. It was concluded that the number and size of defects has decreased after hot-isostatic pressing. Lei Xu et al [47] investigated on effects of hot-isostatic pressing conditions and cooling rate on microstructure and properties of Ti–6Al–4V Alloy. It was found that when HIP treated at 800 °C and at 120 MPa pressure best room temperature tensile strength can be achieved. It known that cooling rate during sintering effects microstructure, but geometry of the samples also can significantly affect microstructure and mechanical properties. Litao Chang et al [48] studied the effect of HIP temperature on microstructure and tensile properties of Inconel 718.

2.5.3 Non- Conventional Consolidation Methods

Non-conventional consolidation methods widely applied to nano-powder densification are microwave sintering and electrical field-assisted sintering. These sintering methods enhance the densification process, thus reducing sintering temperature and time ultimately preserving final fine grain sizes.

Microwave Sintering: Microwave sintering emerged in recent years to meet the demands of powder metallurgy industry for new and improved sintering process. Microwave energy is a form of electromagnetic energy with the frequency range of 3000 MHz to 300 GHz. In this process heating occurs when the materials couple with microwaves and absorb the electromagnetic energy volumetrically and transform into heat. In conventional sintering surface of the material is first heated then the heat moves inward. This leads to temperature gradient between inside and the surface. In the case of microwave sintering the heat is generated inside the material first and spreads to entire volume [49]. Microwave sintering of materials was limited to ceramics, semiconductors, polymer and inorganic materials until the year 2000. However, it has been proven that microwave sintering can be used for consolidating powdered metals also. Advantages of this process are reduced energy consumption, enhanced diffusion processes, rapid heating rates and processing times, decreased sintering temperatures, improved physical and mechanical properties [50-52].

The theory of consolidating metallic materials by an electro-discharge process was proposed in 1960s. Sintering processes developed on this concept which are widely used are:

Pulse plasma sintering (PPS), and

Spark plasma sintering (SPS)

There is no use of external heat source in these processes as in conventional hot pressing. However, a current (DC, pulsed DC, or AC) is allowed to pass through the electrically conducting pressure die and, in appropriate cases also through the sample. This means that the die itself acts as heat source and sample is heated from outside and the inside. The characteristic features of these processes are as follows:

Pulse Plasma Sintering (PPS): In PPS, the material is crossed by intense electrical currents while kept under compressive stress at high temperature, which is locally enhanced through electric pulses. The main feature of PPS lies on the extremely high current of several tens of kA obtained by capacitor discharging. Pulsed DC applied at room temperature for short period of time and continuous DC during remaining sintering process. Many researchers have reported their work on PPS for different materials like Ni_3Al/diamond composites [53], W–Ta composites [54], Diamond–W based coating–Cu composites [55].

Spark Plasma Sintering (SPS): The spark plasma sintering equipment, shown in Fig.2.8, consists of upper and lower punches through which load is applied, graphite die arrangement which contains powder sample to be sintered. The equipment also consists of an electric system which provides pulsed DC current to the powder. SPS systems have many advantages compared to conventional systems like hot-isostatic press, hot press or atmospheric furnaces, such as accurate control and ease of operation.

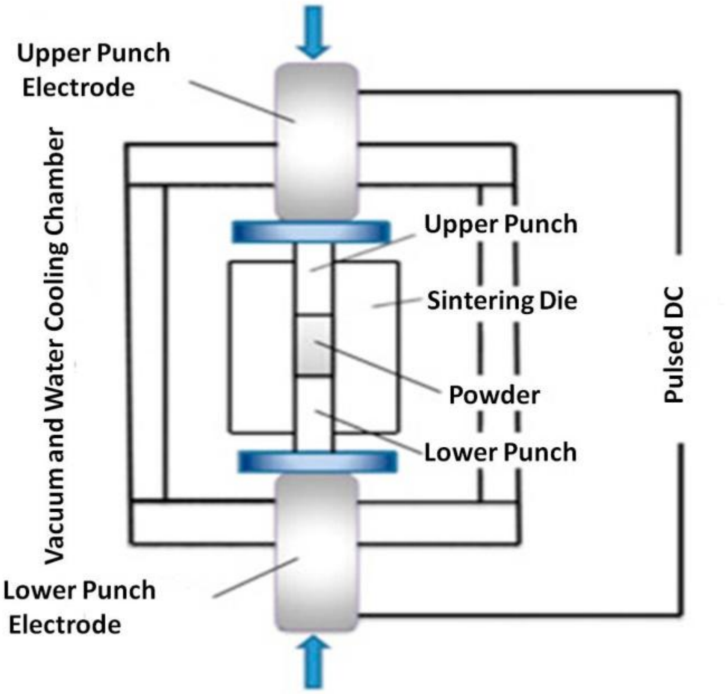

Fig.2.8: Schematic of Spark plasma sintering setup [56].

In this process, a pulsed DC (3.3 ms pulses of 0.5 to 10 kA intensity) is applied from the beginning to the end of sintering cycle. Hence, SPS effect involves simultaneous application of mechanical pressure and high power pulse. Fig.2.9 shows various stages in mechanism of neck formation in SPS process. The pulsed DC current leads to cleaning and surface activation of powders. As soon as the powder surfaces get activated an electric discharge appears in the gap between the powder particles. When the electric discharge appears in the gap between the powder particles, a local high temperature state occurs. This causes vaporization and the melting of the surfaces of the powder particles. During the SPS process constricted shapes or necks are formed around the contact area between the particles. These necks gradually develop and plastic transformation progresses during sintering, resulting in a sintered compact of over 95-99% density. Since only the surface temperature of the particles rises rapidly by self-heating, particle growth of the starting powder materials is controlled. The sintering dies and punches made of graphite are subject to Joule heating according to the progress of the sintering of the internal powder material, and function as heating elements to assume the role of maintaining the homogeneousness of the sintering temperature for the densification [57].

Iwona Sulima et al [58] investigated the effect of SPS parameters on densification and properties of 316 steel matrix composites. It was found that the apparent density of sintered composites depends on sintering temperature and holding time. At higher sintering temperatures high density products, 98-99% of theoretical density, are achieved. In this study SPS holding time did not affect the densification the reason being most of the densification process in SPS will be completed in first few minutes of the process.

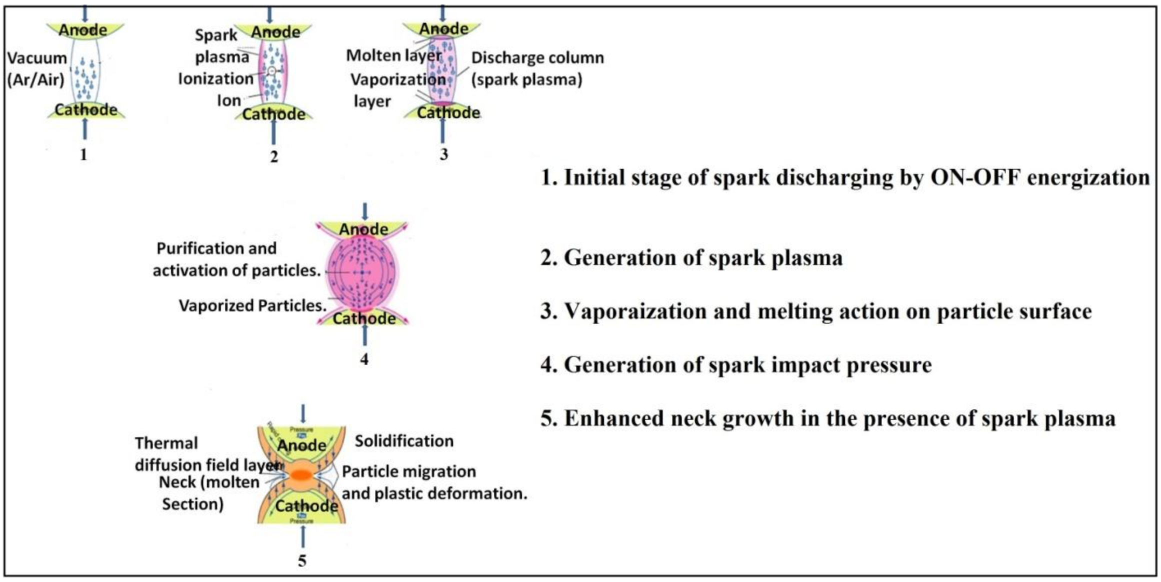

Fig.2.9 various stages in mechanism of neck formation in SPS process

Karthikeyan Rajan et al [59] measured hot-hardness of ODS ferritic steel processed by spark plasma sintering. The microstructure after spark plasma sintering (SPS) consisted of ultra fine grain structure in the size range 310 ± 42 nm and nano-precipitates. High hot hardness was achieved for this steel and hence the combination of mechanical alloying (MA) and SPS was found to give encouraging results.

C. Menapace et al [60] reported bimodal grain structure after MA and SPS in Fe-1.5%Mo with SiC nanoparticles. Full density was achieved at 1050 °C sintering temperature with bainitic ferrite, austenite microstructure. Interestingly the steel displayed ductility although having fine grain structure. High hardness and low yield strength were reported, however the yield strength recorded was greater than typical dual phase microstructured steels. The increased work hardenability makes the material better also than typical (Transformation Induced plasticity) steels in terms of both yield and tensile strength.

Hence from previous research results it can be said that spark plasma sintering is an attractive technique to consolidate nano-structured powders and obtain desired properties.

2.6 Densification of Mechanically Alloyed Powders

Densification of mechanically alloyed powders involves thermally activated transition of powder particle system to thermodynamically more equilibrium state through a decrease of the free surface energy. In solid state densification process decrease in surface free energy is small when compared to other sintering processes. However the distance matter has to be transported is in the order of particle size. The entire sintering process can be divided into three distinct stages, the first stage starts as soon as some degree of atomic mobility is achieved. In this stage sharp concave necks will form between individual particles. About 5% linear shrinkage can be developed during this process. In the intermediate stage, high curvature formed in the first stage have been moderated and microstructure consists of three-dimensional inter penetrating network of solid particles and continuous, channel-like pores. In this stage 5-10% porosity will be persist which covers most of densification. Grain coarsening starts to become important at this stage. Grain coarsening intensity will be high during final stage.

Mechanism of Sintering: Various mechanisms like surface diffusion, vapour transport, lattice diffusion, grain boundary diffusion and dislocation motion, occur during sintering process. Fig.2.10 shows schematic diagram of matter transport paths for two sintering particles. Out of these, surface diffusion and vapour transport do not cause densification. Grain boundary diffusion and lattice diffusion from grain boundary to the neck are the most important densification mechanisms. Neck growth and densification through deformation of particles are caused by plastic flow by dislocation motion which is more common in metal powder sintering.

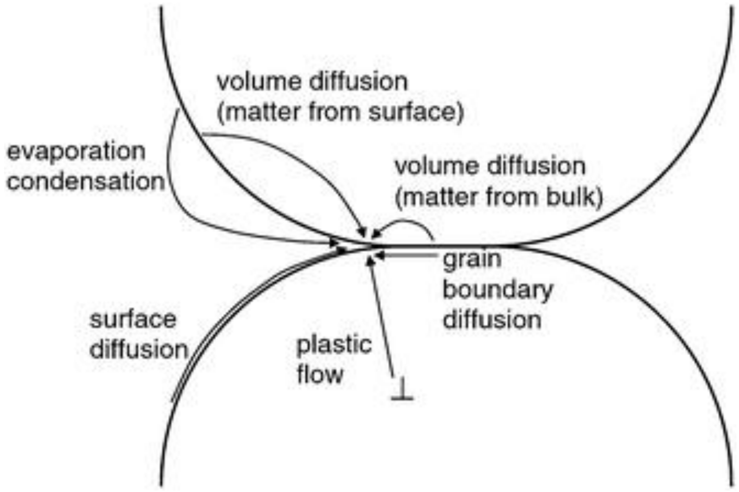

Fig.2.10: Schematic diagram of matter transport paths for two sintering particles [72].

2.7 Strengthening Mechanism in ODS Steels

2.7.1 Matrix Strengthening

The yield strength can be increased by reducing the grain size of the metallic particles. The grain size of the material can be related to yield strength Hall-Petch equation 2.1.

$$\sigma_o = \sigma_i + k\, d^{-1/2} \tag{2.1}$$

Where, σ_I is the "lattice friction stress" which is temperature dependent, k is the Hall-Petch constant, and d is the grain size of the material. K is independent on temperature, composition. As the temperature increases, dislocation recovery processes occur and Hall-Petch effect becomes less effective. This happens because Hall-Petch effect is based on dislocation mechanism. Subsequently weaker deformation mechanism may start to regulate the strength. In fine grained material this results in drop of yield strength at high temperatures. Hence it is desirable to work with materials that possess a stable grain size at high temperatures [61].

2.7.2 Dispersion Strengthening Mechanism

Strengthening in oxide dispersed strengthened austenitic steels is achieved by dispersoid particles acting as barriers to dislocation motion during deformation and as an increasing the load required to tear away to dislocation or bulge it through an array of particles. Strengthening depends on the interactions between particles and dislocations. Finer dispersoids have greater effect on strength than higher volume fraction. Particles hinder dislocations and also apply a retarding force on grain boundaries that tend to migrate. This retarding force per unit area, F_r is given by equation 2.2.

$$F_r = 3 f \gamma_{gb} / 2r \tag{2.2}$$

Where, f is the volume fraction of particles, r is the uniform radius of particles, and γ_{gb} is the grain boundary energy per unit area. From this equation it can be inferred that for certain volume fraction finer the particles greater will be the resistance to grain boundary movement. The strengthening from dispersoids comes from the need to move the dislocations pass the particles [62]. According to Orowan model (Orowan 1946) the resolved shear stress (τ_s) required for dislocation by-pass is given by the equation 2.3.

$$\tau_s = K\,(G\, b/\lambda) \tag{2.3}$$

Where, G is shear modulus of the matrix, b is the magnitude Burgers vector of the dislocation, λ is the inter-particle spacing and K is a numerical constant [19]. To establish a relation between hardness and grain size, if hardness H is assumed to be proportional to the yield strength, it follows equation 2.4 which is

$$H = H_m + k\, d^{-1/2} \tag{2.4}$$

where, H_m - hardness of the matrix and k - Constant. From these equations it is clear that for a fixed volume fraction of dispersed particles, the hardness increases with decreasing particle diameter and for a fixed particle size, hardness increases with volume fraction of dispersoids. Therefore, strengthening is increased if the dispersoids volume fraction is high, powder particles are fine, and distribution of particles is homogeneous. High temperature stability of the particles is necessary for high temperature applications. To take account of the interaction between neighboring dislocations, which had bowed the line energy of the dislocations and the inter-particle spacing Orowan model has been modified. The modified model, equation 2.5, resulted in a reduction of applied stress required for by-passing to occur.

$$\tau_s = K^{'}\,(G\, b/\lambda)\, ln(x/2b) \approx K^{''}\Delta\sigma_o \tag{2.5}$$

where, x is the average diameter of the circle of intersection between the particle and the slip plane, $\Delta\sigma_o$ is the increase in the tensile stress for dispersion strengthened alloys with uniform spherical particles and $K^{''}$- Constant.

2.8 Dislocation - Particle Interaction in ODS Alloys

Pinning of dislocations at hard oxide particles in an ODS alloy can be explained by several theories of the following researchers such as:

1. Orowan bowing of dislocations between particles. This mechanism is for low temperature deformation. However it has been reported that testing at high temperature yielded slightly different results from the Orowan stress for ODS alloys.

2. Another mechanism ‘dislocation smearing’, explains the interactions between dislocations and disjointed dispersoids at elevated temperatures. The dislocation glides up to the particle and moves out over the interface between disjointed particle and matrix. This mechanism relays on diffusive processes and therefore is not likely to function at low temperatures

3. Cross slip becomes less likely to occur when there is decrease in stacking – fault energy. Since Chromium additions decrease the stacking-fault energy in Ni-Cr alloys, cross slip is expected to be unlikely in alloys with high Cr concentrations.

4. Climb over dislocations happens only if there is an attractive force between particles and dislocations. At High temperatures dislocations overcome the oxide particles by thermally activated climb, while at low temperatures where diffusion is slow, dislocation by-pass is assumed to occur by Orowan looping

5. Shearing of particle can take place if a dislocation bows around a particle (soft one), there is possibility for the particle to be sheared.

2.9 Oxidation Behaviour of ODS steels

ODS austenitic steels are potential nuclear structural materials which are believed to be capable withstanding oxidation at high temperatures. Cr content in 304L steel leads to formation of chromium oxide when exposed to high temperatures. This acts as protective layer and stops further oxidation. For the same reason high Cr alloys are used for high temperature applications [68]. Investigations on the effect of grain refinement on oxidation behaviour of austenitic stainless steels were carried out earlier. Austenitic stainless steel, grade 310, containing high Chromium (19-22%) was proposed as a potential candidate for supercritical water- cooled reactor (SCWR) because of its high corrosion resistance at high temperature and high pressure water conditions [63]. Also oxidation behaviour of austenitic stainless steels gets affected by grain size refinement. It is believed that the fine grain structure is responsible for the formation of protective Chromium oxide layer [64].

2.10 Open Questions and Future Scope of Study

The preceding sections discussed that the development of nano oxide dispersed austenitic steels is required to meet high strength materials at room and elevated temperatures for structural and nuclear applications. Few previous investigations on these steels have identified suitable techniques to synthesize desired ODS austenitic steels and also characterize microstructure and mechanical properties. The mechanical alloying technique is a technically viable and potentially promising method for the growing industrial demands for the development of oxide dispersed austenitic steels with better strength both at room and elevated temperatures. Several categories of ODS steels have been developed to meet such industrial demands. However, a lot of research work is still required so as to understand many of the unusual characteristics of the mechanical alloying technique. It is also necessary to develop new ways of sintering and characterization methods to improve and understand mechanical properties respectively.

Hence, the overall scope of the present study will include the synthesis of nano-oxide dispersed austenitic steel by mechanical alloying, characterization of the structure and composition of the milled product, consolidation of the milled powders by conventional sintering and spark plasma sintering as well as studies on the microstructure and mechanical behaviour of the bulk consolidated samples.

.

Chapter 3

Experimental Details

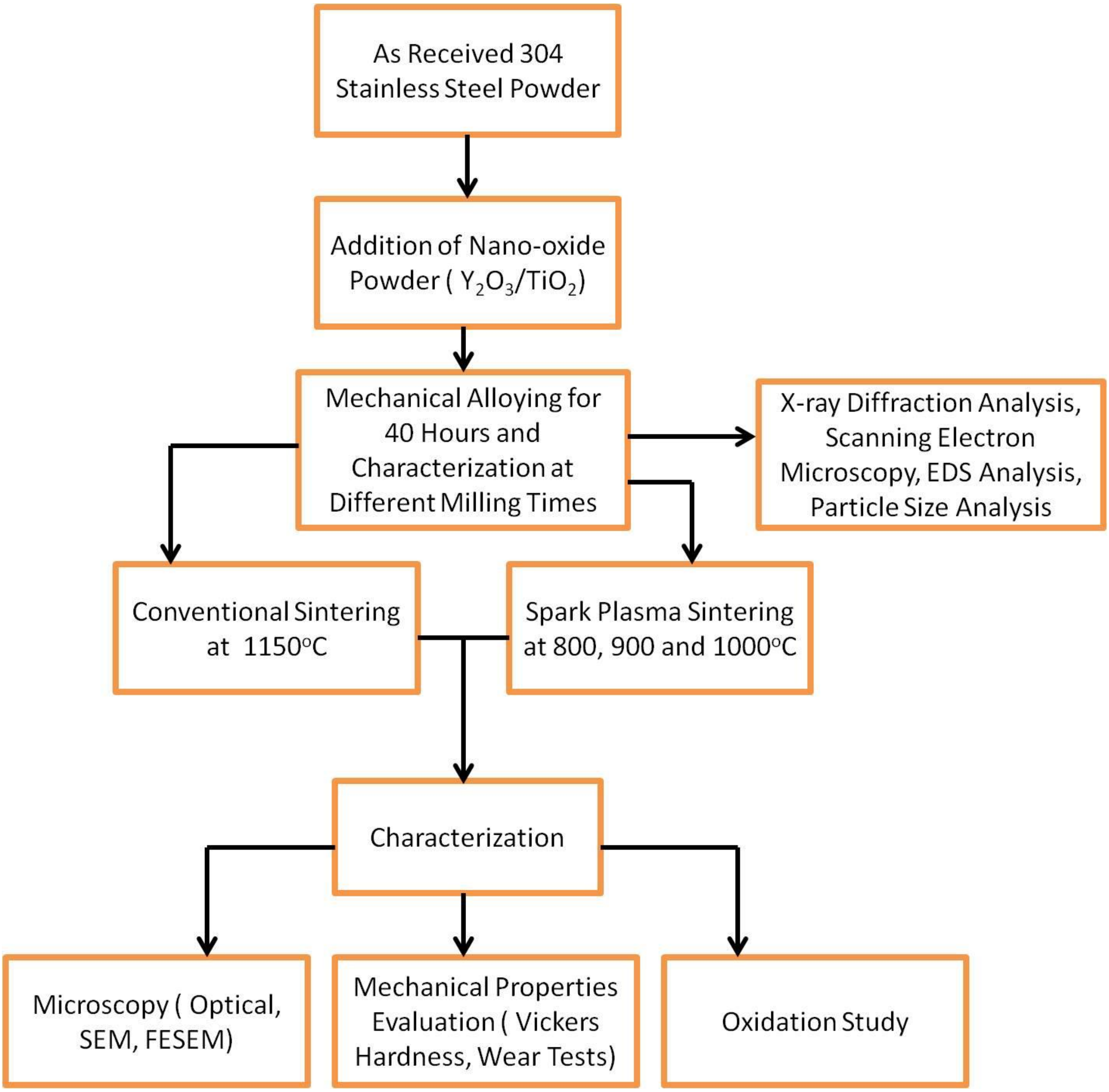

Fig.3.1: Flowchart of series of experiments carried out in the present work

The order of the experiments carried out is as shown in Fig.3.1. Raw materials taken and experimental procedures followed are described in detail in the following sections.

3.1 Raw Materials and Alloy Selection

The raw materials used for the present work are powders of pre-alloyed 304 austenitic stainless steel with size 100 mesh, Yttrium (III) oxide, Reaction, 99.995% (REO) and Titanium (IV) oxide, Anatase, 99.9% (metals basis) from Alfa Aesar. Form and physical properties of the powders are listed in table.

Table 3.1: Details of 304 steel and nano-oxide powders used for producing desired alloys

Material	Size	Density	Melting temperature
Pre-alloyed 304 austenitic stainless steel	100 mesh (< 149 micron)	8.03 g/cc	1454.44 °C
Yttrium (III) oxide	36 nm powder	5.01 g/cc	2410 °C
Titanium (IV) oxide	32 nm APS powder	3.90 g/cc	1855 °C

A total of three different alloys were prepared for mechanical alloying, one base alloy (alloy A) and two nano-oxide dispersed alloys designated as alloy B (1 wt. % Y_2O_3) and Alloy C (1 wt. % TiO_2). Table lists the alloy compositions.

Table 3.2: Chemical compositions of individual alloys in wt. %

Alloy	Powder composition (wt. %)
Alloy A	Fe-19 Cr-11 Ni
Alloy B	(Fe-19 Cr-11 Ni)- 1 Y_2O_3
Alloy C	(Fe-19 Cr-11 Ni)-1 TiO_2

3.2 Mechanical Alloying (MA) of Austenitic Stainless Steels

50 g of pre-alloyed 304 austenitic stainless powders was used for making the alloys with desired compositions. The pre-alloyed powder was divided into two quantities of 25 g each. Two different compositions were produced by adding 0.25 g of Y_2O_3 (1 wt. %) and 0.25 g of TiO_2 (1 wt. %) individually to each of the powder quantities of weight 24.75 g (weighed and taken from 25 g). Weighing of all powders was carried out using a high precision electronic weighing machine with 0.001 g readability. The measured powder quantities of desired compositions were put in individual vials of a planetary ball mil named FRITCSCH, Pulverisette-5. A ball-to-powder ratio of 10:1 is maintained throughout the milling process, i.e. as the powders weigh about 25 g individually, the

grinding media which were chrome steel balls weighing 250 g were introduced in each vial of the ball mill. The mechanical alloying operation was carried out for duration of 40 hours at a rotation speed of 300 RPM. Using these milling parameters and following same procedures a base alloy (alloy A) of composition mentioned in table was milled separately. Samples of the individual alloys were collected at the following intervals of mechanical alloying/milling, 1 h, 5 h, 10 h, 20 h, 30 h, and 40 h, to study phase evolution and changes in particle characteristics. Each alloy powder after final stage of mechanical alloying/milling was consolidated by using spark plasma sintering at temperatures of 800 °C, 900 °C and 1000 °C.

3.3 Consolidation of Alloy Powders

3.3.1 Conventional Sintering

The mechanically alloyed nano-oxide dispersed stainless steel powders were compacted under a uniaxial pressure of 700 MPa for 3 minutes holding time in hardened steel cylindrical die. The green compacts after compaction, were of 15 mm average diameter and 6 mm average height. In the final stage of this consolidation process, the green compacts were sintered at 1150 °C for 60 minutes in a tube furnace with controlled argon gas atmosphere. A constant heating rate of 5 °C/min was maintained and an isothermal hold was allowed for 10-15 minutes at temperatures 1100 °C to ensure uniform temperature distribution in the compacts. The heating cycle followed for spark plasma sintering is shown in Fig.3.2. Characterization of each sintered pellet was carried out by X-ray diffraction analysis, scanning electron microscopy, energy dispersive spectroscopy, ball-on-plate wear tester and Vickers microhardness tester.

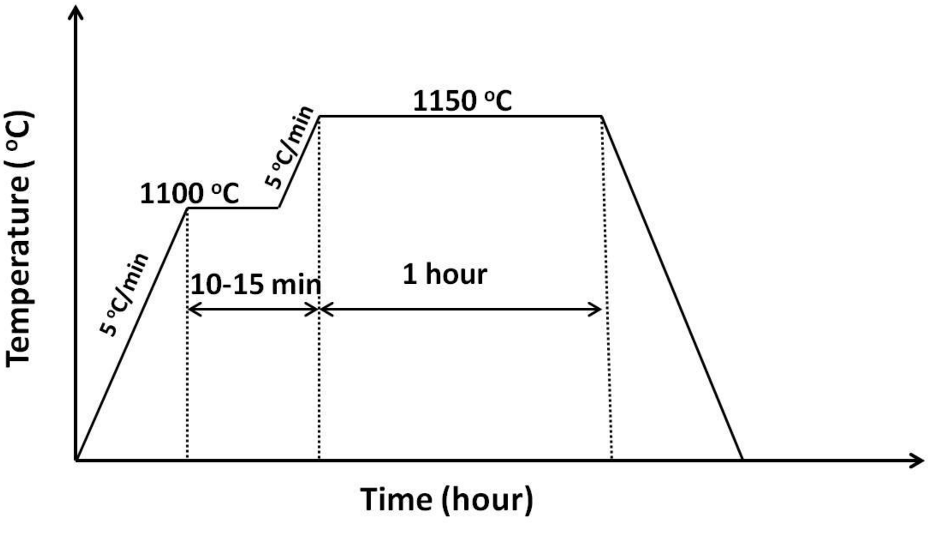

Fig.3.2: Thermal cycle at 1150 °C temperature during conventional sintering

3.3.2 Spark Plasma Sintering

A different set of alloy powders with same compositions and processing conditions as those of powders which were conventionally sintered, were subjected to Spark plasma sintering using SCM 1050, Sumitomo Coal Mining co Ltd., Japan, SPS instrument. The specification of the spark plasma sintering unit used is mentioned in the following table 3.3. The powders were placed inside the graphite die, which was placed between the graphite electrodes of the SPS chamber. Materials were compacted in vacuum in a graphite die with inner diameter 15 mm using a maximum pressure of 30 MPa. Maximum pressure was obtained after 10 min of test duration. Argon was introduced into the SPS chamber which acted as a protective gas and the sintering process was carried out. The alloy powders were sintered at 800 °C, 900 °C and 1000 °C for 5 minutes and a heating rate of 200 °C per minute was used. The heating cycle followed for spark plasma sintering is shown in Fig.3.3.

Table 3.3: Specifications of the spark plasma sintering unit

Current	Voltage	Load	Compact size	Vacuum level	Mould
up to 5 kA	up to 10 V	up to 100 kN	30 mm diameter maximum	up to 6 Pa	Graphite etc.

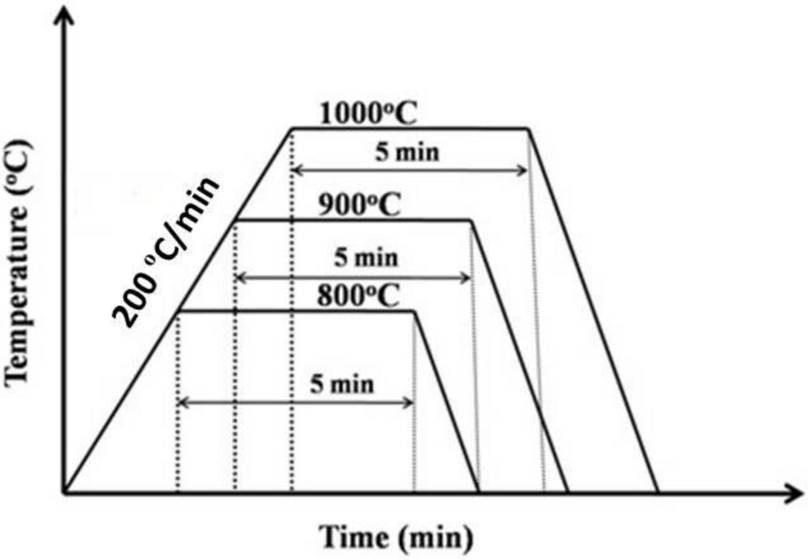

Fig.3.3: Thermal cycle for different temperatures during spark plasma sintering

3.4 Characterization of Powders and Sintered Products

3.4.1 X-Ray Diffraction

Phase identification and evolution of all the alloy powders and sintered products was carried out in Multipurpose X-Ray Diffraction System (Rigaku Japan/Ultima-IV) maintaining a step size of 0.05, for a 2 theta scan range of 20^o to 80^o and a scanning speed of 10^o per minute. The results obtained for each sample are then analysed by X'pert high score plus software. Apart from phase analysis, the crystallite size and residual strain calculations were also made using the X-ray diffraction data. Crystallite size and residual strain of milled powders **(**at 1 h, 5 h, 10 h, 20 h, 30 h, and 40 h**)** were calculated from (111) peak for austenite phase and (110) peak for ferrite phase by using Voigt function [65]**.**

3.4.2 Particle Size Analysis of Powders

The particle size analysis of the milled powders at different stages of milling was done using Malvern - Particle Size Analyzer, U.K. Sample powders of all alloys at 0 h, 5 h, 10 h, 20 h, 30 h, and 40 h of mechanical alloying were individually analysed. Each sample powder was dispersed in ethanol and sonicated for at least 15 minutes before analysis.

3.4.3 Optical Microscopy

Microstructural observation of all the alloy samples was elaborately done using optical as well as electron microscopy. For optical microscopy the sintered pellets surface was first subjected to wheel grinding so as to remove the graphitic and other oxides layers formed. This was followed by belt grinding to obtain a perfectly flat specimen with all the scratches aligned. In the later stage the specimens were polished on a series of emery papers. Fine polishing on diamond impregnated discs was done for required amount of time so as to remove all the superficial scratches and obtain a mirror like surface. Post polishing, the specimens were etched with 5% Nital solution.

3.4.4 Scanning Electron Microscopy and Energy Dispersive X-ray Microanalysis

Microstructural characteristics of milled powders and sintered products were observed under JEOL-JSM-6480 LV scanning electron microscope and field emission- scanning electron microscope, Nova NanoSEM 450. Samples for this purpose were prepared by similar procedures which were followed for optical microscopy. Elemental analysis and mapping of each phase in the observed microstructures was done using Energy Dispersive Spectroscopy (EDS) analysis, which equipment is attached to the scanning electron microscope. Through EDS analysis an estimation of elemental distribution in different phases was obtained.

3.4.5 Density and Porosity Measurement

Archimedes principle was used to measure the density of consolidated samples. The immersion medium was distilled water (density 1 g/cc) and its temperature was maintained within 24 ± 0.3 °C. The following equation was used to calculate densities:

$$\rho_{air} = \frac{W_a}{(W_a - W_w)}(\rho_w) \tag{3.1}$$

ρ_{air} = Densityof sample in air, Wa = Weight of sample in air, Ww = Weight of sample when immersed in water, ρ_w = Density of Water.

At least three density measurements were taken for each sample to obtain a precise and reliable value and minimize error. Theoretical densities of alloys calculated from rule of mixtures and the measured experimental densities were used to determine porosity (%) in consolidated samples.

3.4.6 Hardness Measurement

Vickers hardness of all the sintered specimens was evaluated using LECO (LM248AT) micro-hardness tester at a load of 50 gf and for a dwell time of 10 s. The Vickers hardness has been calculated using the expression:

$$HV = \frac{1.854\,P}{(d_{avg})^2} \quad kgf / mm^2 \tag{3.2}$$

Where, P = Applied load, d_{avg} = Average length of indentation diagonal. A minimum of 10 hardness readings were taken for each specimen along its diameter.

3.4.7 Wear Behavior Study

The equipment used for wear behaviour study was DUCOM TR-208-M1 ball on plate type wear testing instrument, schematic shown in Fig.3.4, having a diamond indenter. The device was operated at 20 RPM and 20 N load for 5 min at the ambient temperature (22–25 °C) and humidity (50-55%).

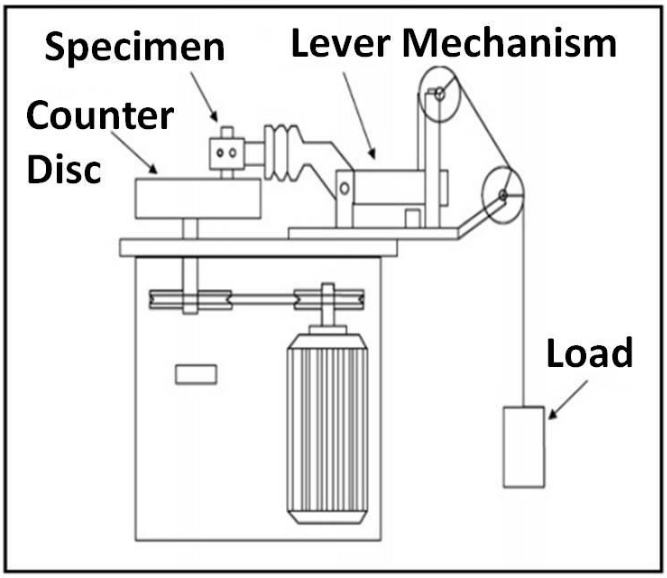

Fig.3.4: Schematic of wear testing equipment

3.4.8 Oxidation Study

Cylindrical Specimens consolidated by spark plasma sintering were used for oxidation tests. The tests were conducted inside a vertical tube furnace in dry air atmosphere at 1000 °C temperature for up to 50 h. Of all the sintered samples highest density was achieved for alloys sintered at 1000 °C. Hence to better understand the behaviour of present 304 austenitic stainless steel, 1000 °C temperature was used. The samples used for the test were polished on all sides starting with medium and fine abrasive papers followed by fine polishing on diamond impregnated discs. The vertical tube furnace equipment consists of a mechanical mass balance, with a least count of 0.1 mg in-built in it facilitating to record the mass of samples at different time intervals between 0.5 to 5 h at a particular temperature. The furnace is equipped with a quartz tube of 5 cm diameter which is surrounded by insulation and SiC heating rods. To maintain a gap of approximately 0.15 m between the mechanical mass balance and the top end of quartz tube, the mass balance was positioned on a steel support frame. The test samples wrapped in platinum wire were so arranged in the furnace such that one end of the wire is hooked to the weighing pan and the other end with the sample was inside the hot zone of the furnace.

Chapter 4

Results and Discussion

4.1 Synthesis and Characterization of Powders

4.1.1 Phase Evolution during Mechanical Alloying

Fig.4.1 (a) shows X-ray diffraction patterns of alloy A (70.0Fe-19.0Cr-11.0Ni) powder at different milling times. It is relevant that the high intensity austenitic peak of unmilled (0 h) alloy A powder is very sharp in nature in the initial stages of milling then gradually decreases and broadens as milling time increases. The presence of new ferritic peaks at 2θ = 44° and 65° after one hour of milling depict the transformation of some amount of austenite phase to ferrite. It can be observed from the patterns that upon further milling i.e. beyond 5 h, the peak broadening is more significant. This is due to the fact that the crystallite size decreases with increasing milling time which leads to peak broadening. Increase in full-width at half-maximum (FWHM) with increasing milling time depict that both plastic strain build up and reduction in crystallite size are occurring.

X-ray diffraction results obtained from alloy B (69.0Fe-19.0Cr-11.0Ni-1.0Y_2O_3) and alloy C (69.Fe-19 Cr-11 Ni-1.0TiO_2) powders at different milling times from 1 h to 40 h are shown in Fig.4.1 (b) and Fig.4.1 (c) respectively. After 1 h of milling, there is a sharp peak at around 2θ = 44° corresponding to (110) plane of ferrite indicating the existence of ferrite along with austenite in the alloy matrix. There is gradual reduction in sharpness and intensity of the ferritic and austenitic peaks with increase in milling time and also the intensity of ferritic peak at around 2θ = 65° disappeared after 10 h of milling.

The XRD patterns of alloy C powder were found to be not very different from those of alloy A and alloy B powders. Because of the fact that stain-induced transformation from austenite to ferrite had occurred after 1 h of milling. There exists similarity between the two oxide dispersion strengthened alloys (alloy B and alloy C) that the number of ferritic peaks reduced after 10 h of milling and the same peak at around 2θ = 44° gradually broadens and almost merges with the adjacent austenitic peak with increasing milling time. Strain-induced transformation of similar kind from austenite to ferrite was reported earlier by Man Wang et al [24]. In which similar MA was performed but with higher amounts of Y_2O_3, pure Ti and lower Ball-to-powder weight ratio i.e. 5:1. Hence it is possible that the extent of strain-induced transformation depends on the amount of alloying additions and milling parameters. The processes namely plastic strain build up and crystallite size reduction were observed to be common during mechanical alloying (MA) of all the three alloys.

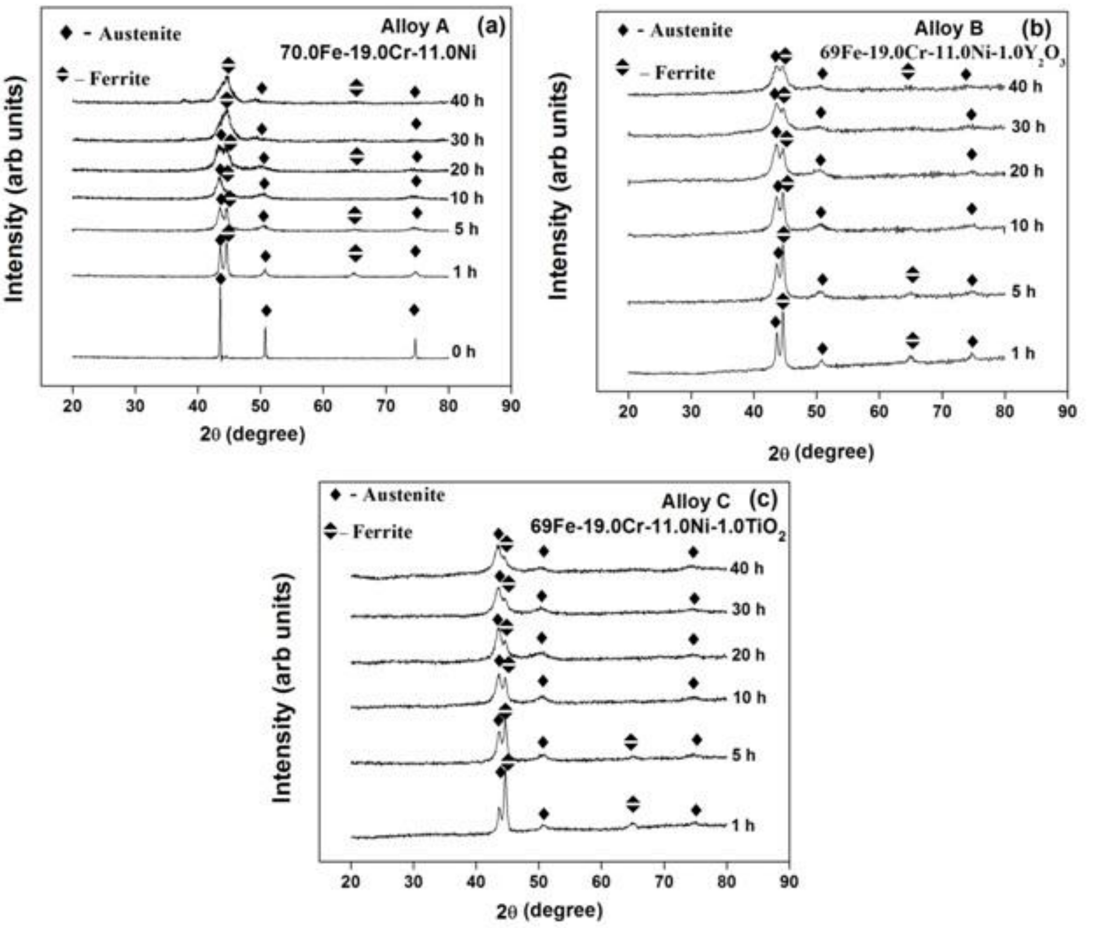

Fig.4.1: X-ray diffraction profiles of (a) alloy A, (b) alloy B, (c) alloy C subjected to mechanical alloying up to 40 h

4.1.2 Morphology and Size of Powder Particles during Milling

Fig.4.2 shows scanning electron micrographs (SEM) of unmilled (0 h) and milled alloy A powders at different time intervals (0 h, 5 h, 10 h, 20 h, 30 h and 40 h). It is clear from the images that there is substantial variation in morphology and size of the powder particles during the course of milling. It is found that powder particles at unmilled condition (0 h) shown in Fig.4.2 (a) are irregular in shape and larger in size. During the early stages of milling, the stainless steel powder particles are soft and ductile. Soft particles have tendency to weld together and form particles of larger sizes. As milling continues, the ductile nature of the austenitic stainless steel powder particles leads to particle agglomeration and after completing 5 h of milling the size of the powder particles get reduced and also these particles get flattened. At the later stages of milling, the flat powder particles lamellae weld together to form a single large lamella. It was observed that powder particles milled at 10 h are more spherical in shape and their size distribution is uniform. Apparent particle size of 10 h milled product was analyzed by SEM micrograph and the average particle size values are summarised in Table 4.1. It may be demonstrated that there is a possibility of work hardening phenomenon in the sub-micron size particles from 10 h to 20 h of milling.

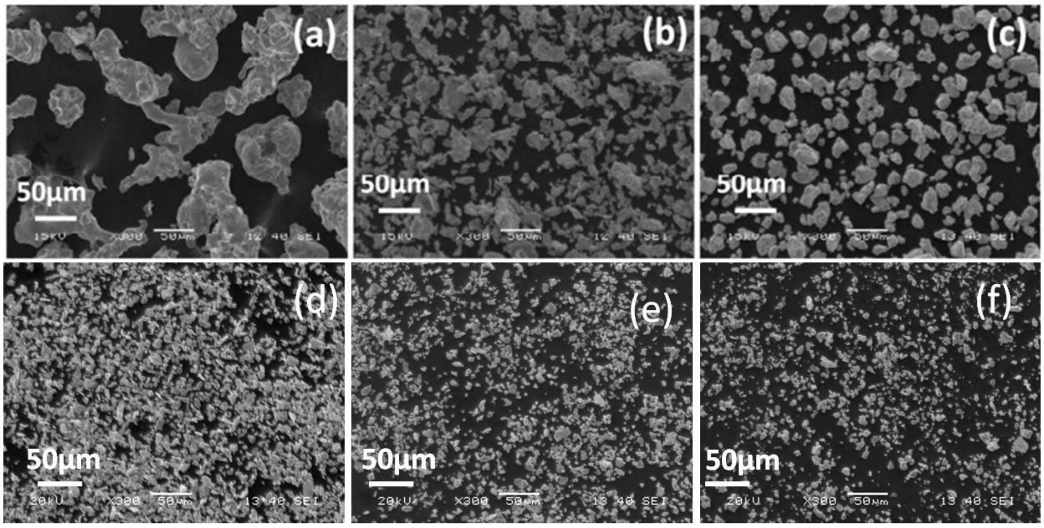

Fig.4.2: FE-SEM micrographs of alloy A powder at different milling times (a) 0h, (b) 5 h, (c) 10 h, (d) 20 h, and (e) 30 h, (f) 40 h

The increase in residual strain with milling time can be directly related to increase in work hardening of the powder particles. Increase in work hardening is linear up to 30 h of milling as a result the particles gradually lose ductility and becomes brittle in nature. Plastic deformation and subsequent work hardening have lead to fatigue and fragmentation of brittle powder particles. Work hardening of powder particles during milling was reported earlier by Shashanka et al [31]. Beyond 30 h of milling although there was no significant change in powder morphology, average size of the particles was reduced from 20.58 µm to 5.12 µm. Compared to other milling times, the minimum to maximum size variation of the powder particles was found to be least after 40 h milled condition. Hence it can be suggested that particle size distribution upon 40 h of milling is relatively more uniform as compared to the previous milling stages. Small particle size helps in improving densification of the powder due to large surface to volume ratio.

Initially the average particle size is about 50 µm, and then it reduced to 3.5 µm after 40 h milling. Although the flaky nature of the particles was retained after milling, the morphology of powder particles has changed such that in the initial stages of milling the particles appear in group and overlapping on one another. While in later stages, as milling times increases the finer particles can be individually distinguished**.**

Table 4.1: Average particle size of milled powder (Alloy A) at different milling times

	Particle size (µm)	
Milling time	Particle Size Analyzer	Image analyzer
(a) 0h	50.86 ± 6.19	39.24 ± 4.19
(b) 5 h	32.25 ± 5.82	29.00 ± 4.03
(c) 10 h	20.58 ± 4.23	16.49 ± 3.59
(d) 20 h	10.53 ± 3.46	9.68 ± 2.55
(e) 30 h	5.12 ± 2.09	4.16 ± 2.01
(f) 40 h	3.50 ± 1.96	3.41 ± 1.75

4.1.3 Crystallite Size and Residual Strain Calculations

The data from X-ray diffraction spectrums of all alloy powders at different stages of milling were used for theoritical calculations of their crystallite sizes. Table 4.2 lists Crystallite Size (nm) and Residual strain (%) values at different milling times (h) calculated by using Williamson–Hall equation (Equation 4.1),

$$\beta \cos\theta = (\frac{0.94\lambda}{D}) + 4\eta \sin\theta \tag{4.1}$$

where D is the crystallite size, β - FWHM and θ - bragg angle, measures average nano-crystallite size, λ - wave length of X-rays, η - strain. The gradual increase in full-width at half maximum (Δθ) as milling time increases indicates the reduction in crystallite size and residual strain build up have happened. Crystallite sizes calculated from full-width half maxima (FWHM) of the high intesity peak of each individual spectrum of alloy A, alloy B and alloy C are shown in Fig.4.3 (a), (b), and (c) respectively. Instrumental broadening measured from X-ray diffraction patterns of pure silicon i.e. the β_{standard} (Si 111) value was 0.18 (°2θ). Profile fitting in the X'pert high score plus software fits Pseudo-Voigt profile function to the measured data, this has also deconvoluted the overlapped peaks and hence more reliable peak parameters were obtained.

Table 4.2: Crystallite Size (nm) and Residual strain (%) values at different milling times (h)

Milling time (h)	Crystallite Size (nm)			Residual strain (%)		
	Alloy A	Alloy B	Alloy C	Alloy A	Alloy B	Alloy C
0	437.00	459.00	416.00	0.03	0.23	0.15
1	138.00	142.73	178.20	0.15	0.37	0.93
5	40.85	52.10	53.00	0.17	0.57	1.72
10	22.87	27.45	26.00	0.32	0.65	2.38
20	18.33	16.86	14.00	0.49	0.81	2.65
30	14.03	15.86	9.00	0.72	0.98	2.88
40	11.73	9.51	7.00	0.76	1.19	3.21

$$\beta_{structural} = \beta_{observed} - \beta_{s\tan dard} \tag{4.2}$$

To calculate their average crystallite sizes equations 4.1 and 4.2 were used. The average crystallite size of before milling alloy A was 437 nm while after 40 h of milling it decreased to 11.73 nm. The calculated average crystallite sizes of ODS alloys alloy B and alloy C after 40 h of milling are in the range of 7 to 10 nm. Residual strain induced was found to be more in the alloy C powders and least in alloy A powders. These results confirm that the addition of 1 wt. % nano-oxides can affect the crystallite size and residual strain of the alloy powders during the course of milling.

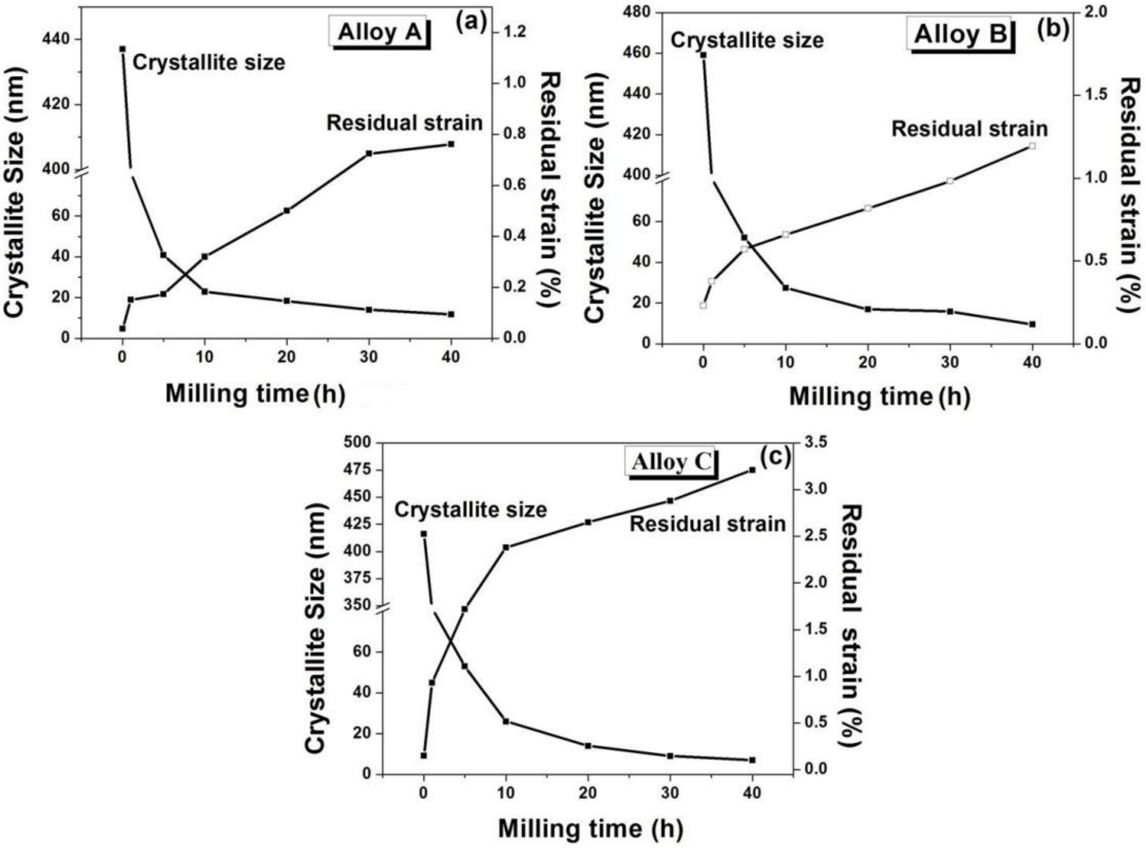

Fig.4.3: Variation in crystallite size (nm) and residual strain (%) with increasing milling time (h) of (a) alloy A, (b) alloy B, and (c) alloy C powders

4.1.4 Compositional Micro-analysis of Powders by EDS

Electro dispersive spectroscopy (EDS) analysis results of alloy powders after milling them up to 40 hours are shown in Fig.4.4. The elemental proportions of Fe, Ni and Cr are in conformity with the initial powder composition taken before milling, Fig.4.4 (a). Fig.4.4 (b) consists of small peaks of yttrium and oxygen confirming the presence of Y_2O_3 in the milled alloy B powder. Similarly, the peaks of titanium and oxygen in (EDS) spectrum of alloy C Fig.4.4 (c) stand as evidence for TiO_2 presence. No sign of intermetallic phases of Fe, Ni or Cr with yttrium or titanium was observed in X-ray diffraction analysis, shown in Figs.4.1 (a), (b), and (c). Hence, the yttrium and titanium in the alloys B and alloy C respectively should exist as initially added nano-oxides. Table 4.3 summarizes the EDS analysis of powders mechanically alloyed for 40 h.

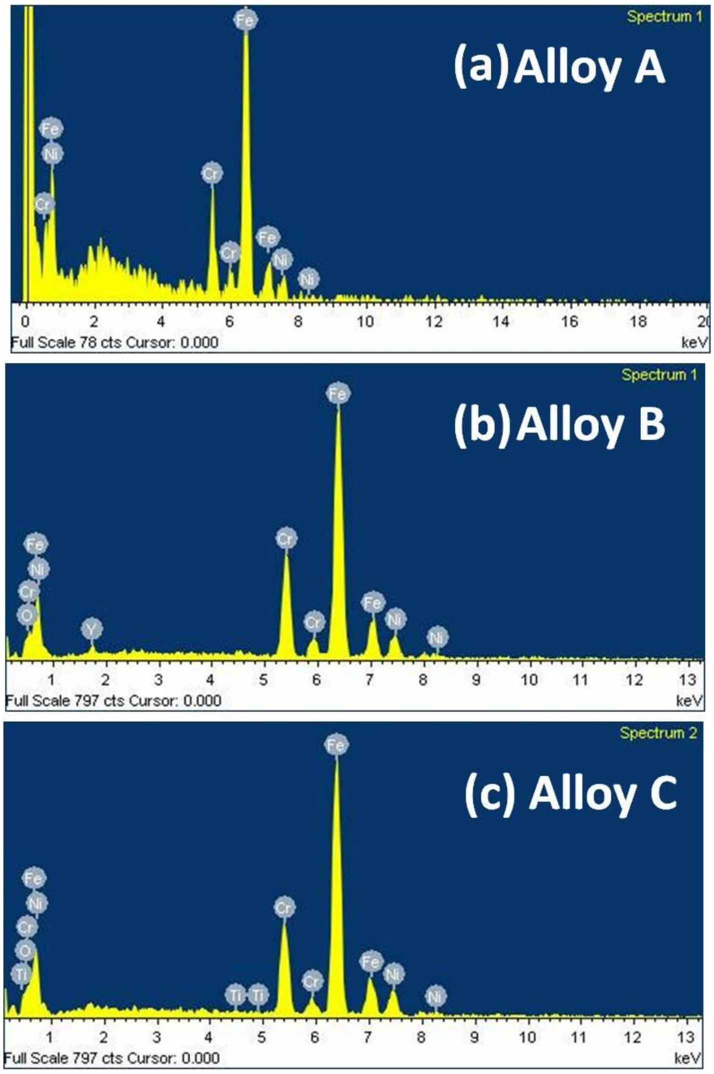

Fig.4.4: EDS spectrums of 40 h mechanically alloyed powders of (a) alloy A, (b) alloy B and (c) alloy C

Table 4.3: Summary of EDS analysis of 40 h mechanically alloyed powders

Alloy	Elements (wt %)					
	Cr	Ni	Ti	Y	O	Fe
A	19.40	10.96	-	-	0.03	Balance
B	19.29	10.92	-	0.37	0.54	Balance
C	19.21	10.94	0.58	-	0.38	Balance

4.2 Characterization and Properties Evaluation of Sintered Products

4.2.1 Conventionally Sintered Products

Phase Identification by XRD Analysis

Fig.4.5 shows the XRD patterns of alloy A, B and C respectively, sintered at 1150 °C for 1 hour in Ar atmosphere. It reveals that the presence of predominant austenite phase and also the presence of ferrite phase. Similar, kind of observation has been found by Shashanka R et al [66]. The patterns suggest no formation of intermetallic in alloy A and alloy B but Ni_3Ti intermetallic peak was obtained for alloy C after sintering. The austenitic peaks obtained are of high intensity and sharper indicating substantial grain growth and perfect crystallographic orientation. In summary, by X-ray diffraction analysis the phases found in each alloy are as follows: Alloy A- austenite and, ferrite, Alloy B- austenite, ferrite and, Y_2O_3, Alloy C- austenite, ferrite, TiO_2 and, Ni_3Ti.

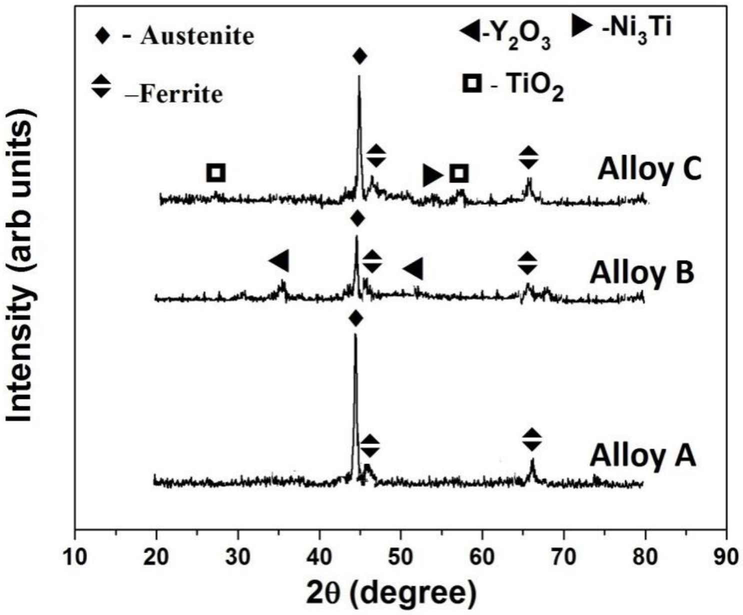

Fig.4.5: X-ray diffraction patterns of conventionally sintered (at 1150 °C) Alloy A, Alloy B and Alloy C

Microstructural Evolution by SEM and EDS

Figs.4.6 (a), (b) and (c) show the FE-SEM micrographs of the sintered pellets of alloy A, alloy B and alloy C respectively. Throughout the microstructures of all three alloys a combination of bright and dark phase is present. The XRD results (Fig.4.5) also confirms the presence austenite and ferrite phases in the sinteted pellets. From the EDS analysis of alloy A (Table 4.4), it was found that the bright areas are Ni-rich (austenite phase) and dark areas are Cr-rich (ferrite phase). The summary of EDS analysis of bright and dark phases present in alloy A are tabulated in Table 4.4.

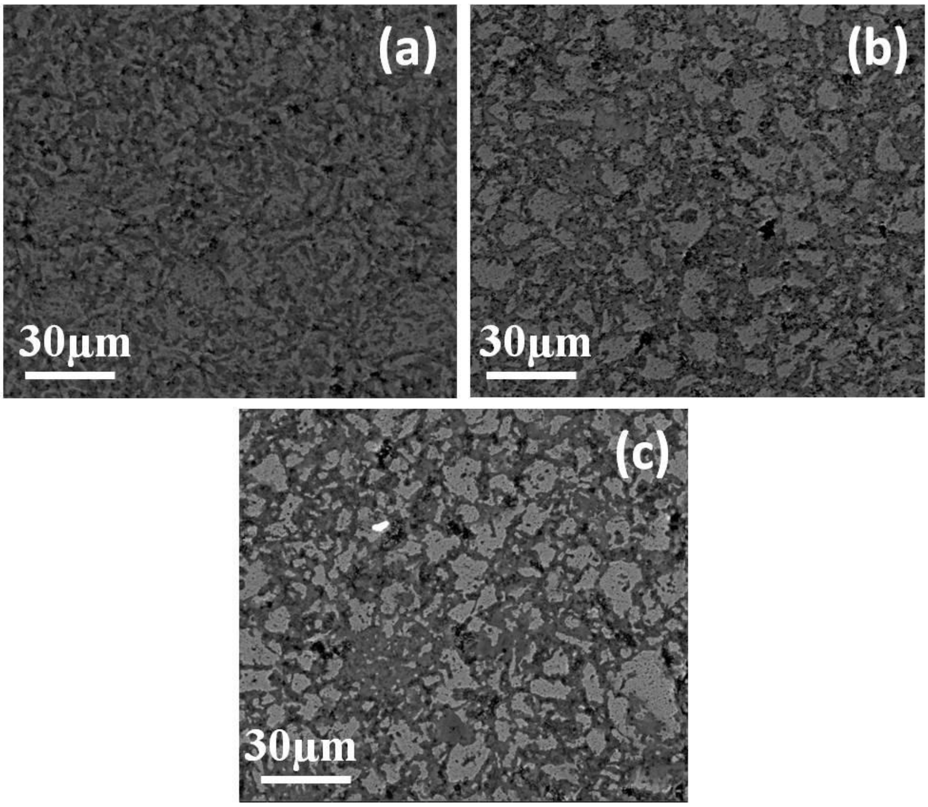

Fig.4.6: FE-SEM micrographs of (a) alloyA, (b) alloy B, (c) alloy C conventionally sintered at 1150°C for 1 h

Fig.4.7 shows EDS patterns of sintered alloy A (a), alloy B (b) and alloy C (c). It is observed that there is variation in volume fraction of Ni-rich and Cr-rich phases in the three alloys. The variation in volume fraction of Ni and Cr- rich phases as observed in Fig.4.7 is due to the fact that any kind of sintering process is diffusion controlled process which depends on time, temperature and diffusion coefficient of the constituents. During sintering, diffusion of Ni and Cr in austenitic stainless steel may alter because the diffusion coefficients of Ni and Cr are different. As a result of that there is pretty chance of the formation of Ni rich and Cr-rich phase in materials. As the alloys are different, the volume fraction of Ni and Cr rich phase will be different. Apart from presence of Fe, Cr, and Ni Figs.4.7 (b) and (c) show presence of Y, O and Ti, O respectively.

Table 4.4: Summary of EDS analysis of bright phase and dark phase in alloy A

Elements	Bright Phase wt. %	Dark Phase wt. %
Fe	72.96	73.17
Cr	8.81	23.08
Ni	18.23	3.75

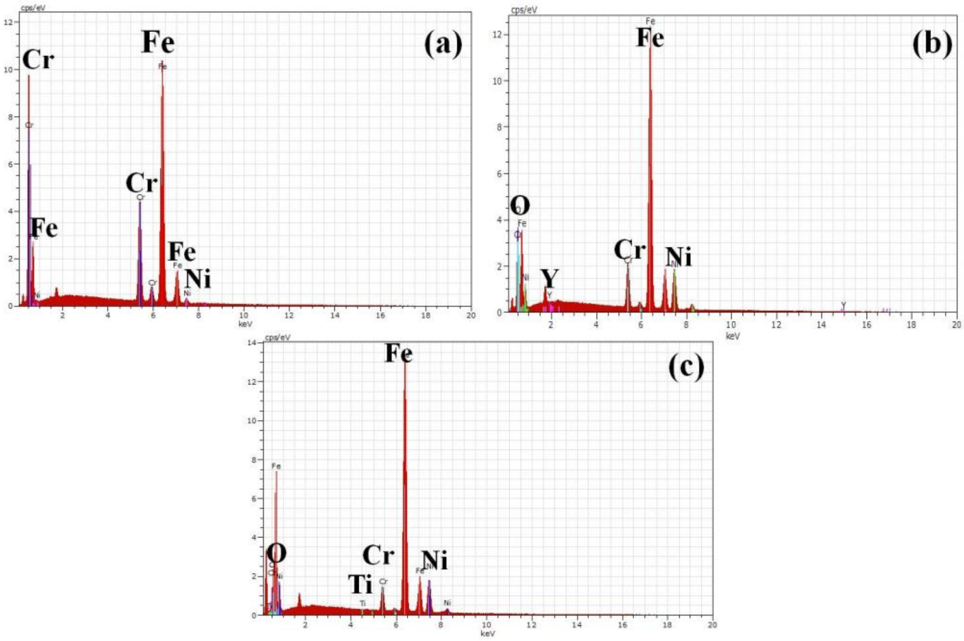

Fig.4.7: EDS patterns of (a) alloy A, (b) alloy B, (c) alloy C processed by conventional sintering

4.2.2 Spark Plasma Sintered Products

Phase Identification by XRD Analysis

Figs.4.8 a-c, show the XRD patterns of the three alloys consolidated by spark plasma sintering at 800, 900 and 1000 °C. It reveals that the presence of predominant austenite phase and also ferrite phase for all the alloys at different sintering temperatures. Furthermore, the presence of Y_2O_3 and TiO_2 phase were identified in alloy B and alloy C, respectively. Also, Fig.4.8(c) reveals the presence of nickel-titanium intermetallic (Ni_3Ti) in alloy C. During sintering, there is a chance of formation of Ni-Ti intermetallic because Ti is reactive element which comes from its partial diffusion from TiO_2 and also it has a great affinity towards Ni. So there is a possibility for Ni-Ti intermetallic formation during sintering. On the other hand yttrium from Y_2O_3 is not so reactive, thermodynamically more stable, to form any intermetallic with Ni.

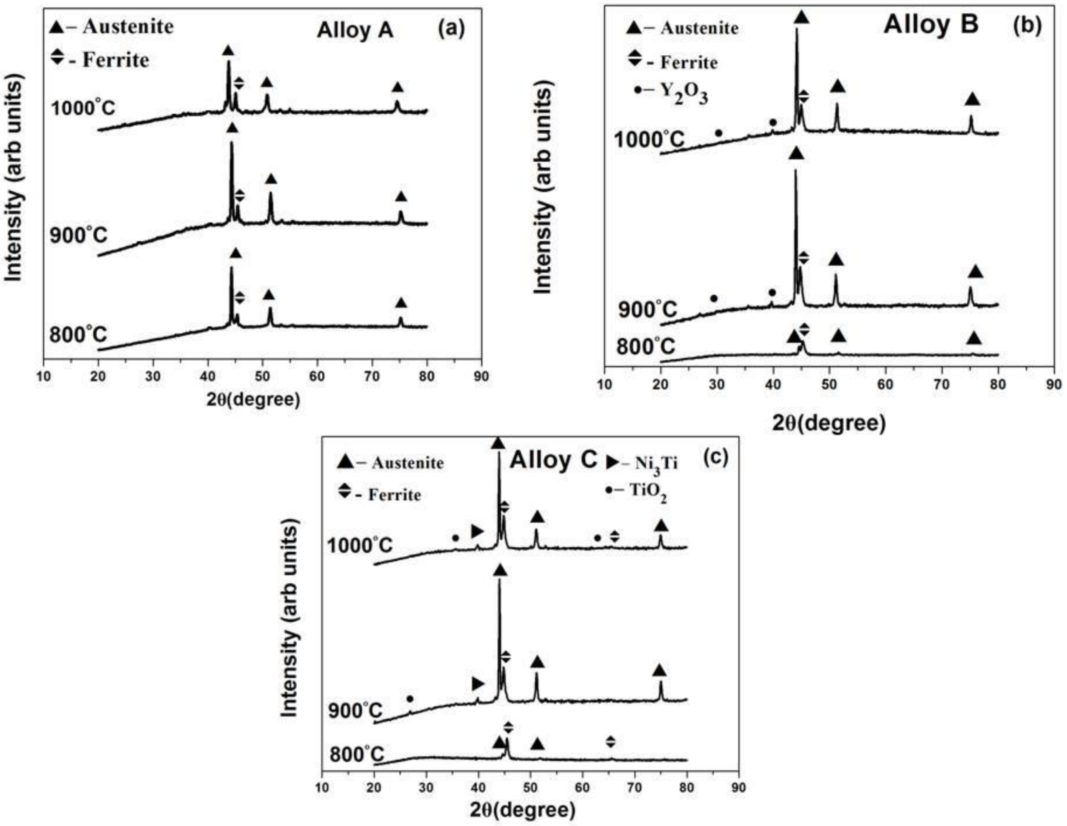

Fig.4.8: XRD patterns of samples sintered by spark plasma sintering (SPS) at different temperatures: (a) alloy A, (b) alloy B, and (c) alloy C

Microstructural Evolution by SEM and EDS

Figs.4.9a-c show scanning electron micrographs of alloy A consolidated at (a) 800 °C, (b) 900 °C, and (c) 1000 °C by spark plasma sintering. From Fig.4.9a it is clear that there is porosity (dark regions) in all the microstructures. By close observation dark and bright phases can also be distinguished in the micrographs similar to that of samples sintered by conventional sintering (Fig.4.6) but are only fine in size. XRD analysis (Figs.4.8a-c) also confirmed the presence of austenite phase and ferrite phases in the alloy. From EDS spectrums shown in Figs.4.12a-b, it was confirmed that the dark phase belongs to ferrite and bright phase belongs to austenite. Furthermore, the microstructures reveal that the sample sintered at 800 °C shows the minimum density or maximum area fraction of porosities in the microstructure which is attributed to incomplete grain bridge formation or welding at relatively low temperature resulting in partial sintering of the sample.

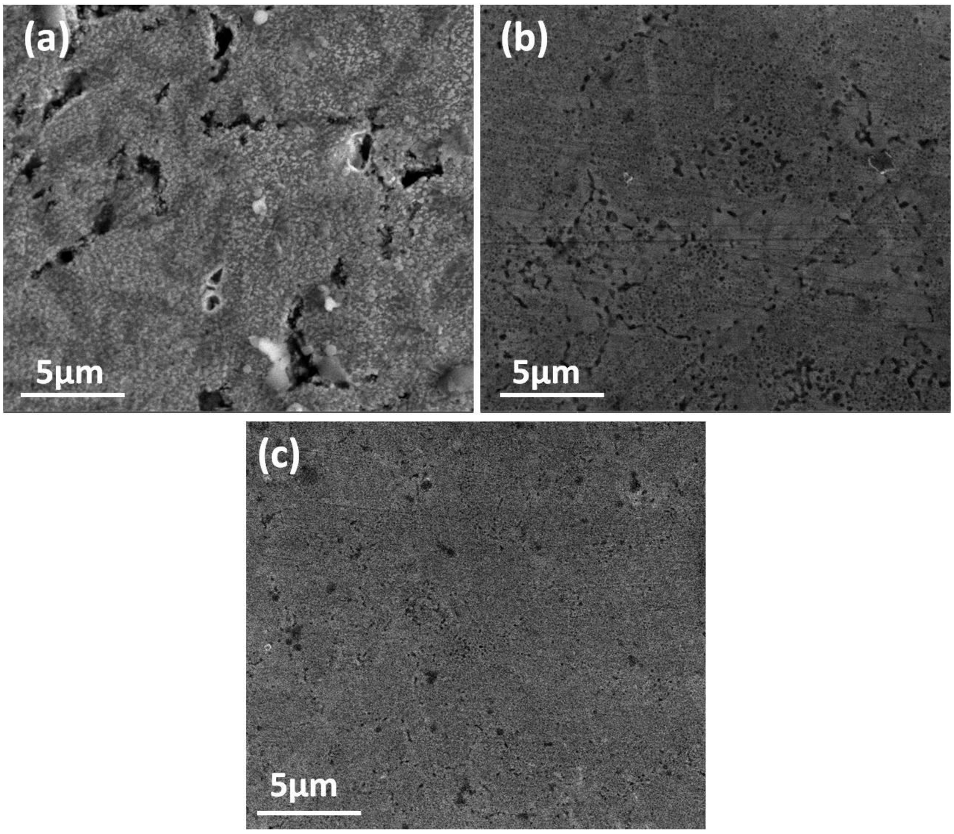

Fig.4.9: Scanning electron micrographs (FE-SEM) of alloy A processed by spark plasma sintering at (a) 800 °C, (b) 900^{o}C, (c) 1000 °C

Similar trend was observed in microstructures of alloy B and alloy C shown in Figs.4.10 and 4.11 which consist of bright phase, dark phase the black spots are pores. Also, from Figs.4.10 and 4.11 it is clear that the pores lose continuity which is observed in microstructure of samples sintered at 800 °C (Fig.4.10a and Fig.4.11a) and become smaller as the sintering temperature increases. This reduction in porosity can be attributed to higher extent of pore closure occurred in the alloys sintered at higher temperatures.

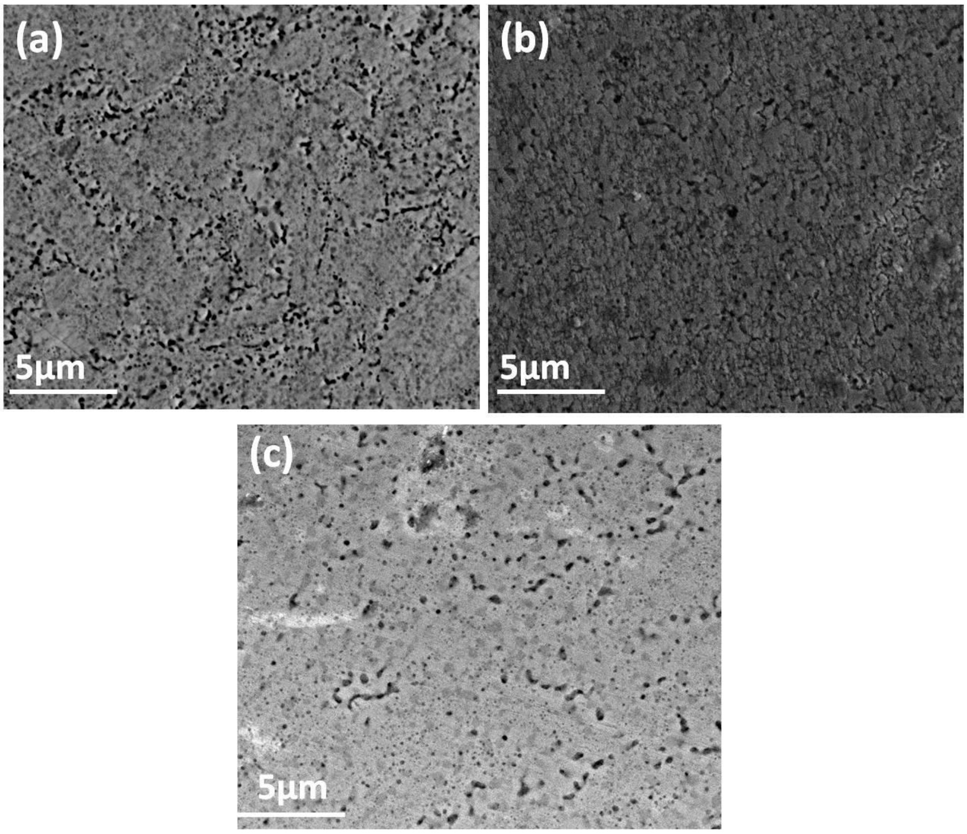

Fig.4.10: Scanning electron micrographs (FE-SEM) of alloy B processed by spark plasma sintering at (a) 800 °C, (b) 900°C, (c) 1000 °C

The austenite and ferrite phases as obtained by XRD analysis of the sintered samples (Fig.4.8) are uniformly distributed in the microstructure of all the alloys which can be clearly observed in Fig.4.10c. Figs.4.12a-b show EDS spectrums of bright and dark phases in alloy A, which are of austenite and ferrite respectively. These findings are similar to that of conventionally sintered alloys with little variation in relative amounts of Fe, Cr, and Ni.

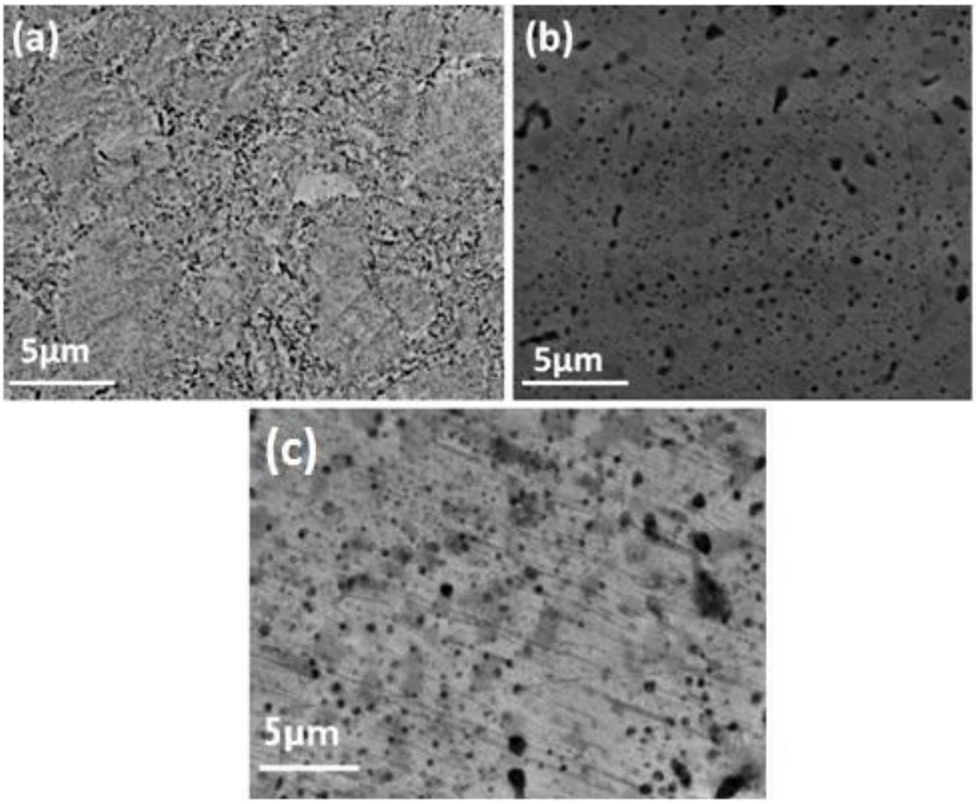

Fig.4.11: Scanning electron micrographs (FE-SEM) of alloy C processed by spark plasma sintering at (a) 800 °C, (b) 900 °C, (c) 1000 °C

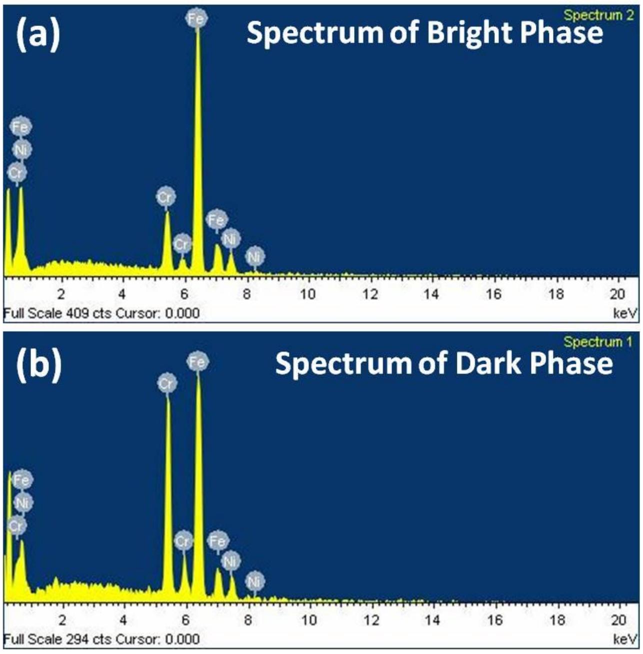

Fig.4.12: EDS spectrums of (a) bright phase and (b) dark phase in spark plasma sintered alloy A

As mentioned earlier the EDS spectrums of bright phase and dark phase reveal the elemental proportions of Fe, Cr, and Ni in wt.%. The micro-compositional analysis by using EDS spectrum of bright phase and dark phase of alloy A are summarized in Table 4.5.

Table 4.5**:** Summary of EDS analysis of bright phase and dark phase in SPS alloy A

Elements	Bright phase Wt. %	Dark phase Wt. %
Fe	74.97	71.38
Cr	9.45	20.92
Ni	15.58	7.70

4.2.3 Evaluation of Physical and Mechanical Properties of Consolidated Products

Physical Properties

Figs.4.13a and b show variation of bulk density and porosity of the sintered samples, measured using Archimedes principle, as a function of sintering temperature for all three alloys. From the density values of conventionally sintered samples, Fig.4.13a, it was found that the maximum density is achieved for alloy C and minimum density for alloy A. From Fig.4.13b it is evident that density increases with increase in sintering temperature for all the SPS alloys. The bulk density and porosity values of all the three sintered alloys by conventional sintering and SPS, measured using Archimedes principle, as a function of sintering temperature are summarized in Table 4.6. It clearly reveals that a maximum density of 7.77g/cc was attained for SPS alloy C by sintering at higher temperature i.e. 1000 °C. Relatively low density at lower temperature is because of incomplete diffusional bonding. Previous investigations have reported dependence of density on sintering temperature and that increase in sintering temperature would lead to enhanced diffusion [25]. Kerry N. Allahar et al [67] also have reported the influence of sintering temperature on relative density values of alloys milled for 40 h duration and consolidated by spark plasma sintering. In which, it was found that, particularly the consolidated samples of the powder milled for 40 h were most influenced by sintering temperature among unmilled (0 h) powder and 20 h milled powder. Density values of conventionally sintered alloys (6.57 - 6.89 g/cc) are lower than those of SPS alloys (7.06 - 7.77 g/cc). The maximum density of alloy C processed by spark plasma sintering is attributed to the continuous application of pressure (30 MPa) at high temperature during the sintering process. As a result samples processed by SPS for 5 min were densified greater than 90% but samples that sintered by conventional method for longer duration, 1 h, in furnace achieved only nearly 85% densification.

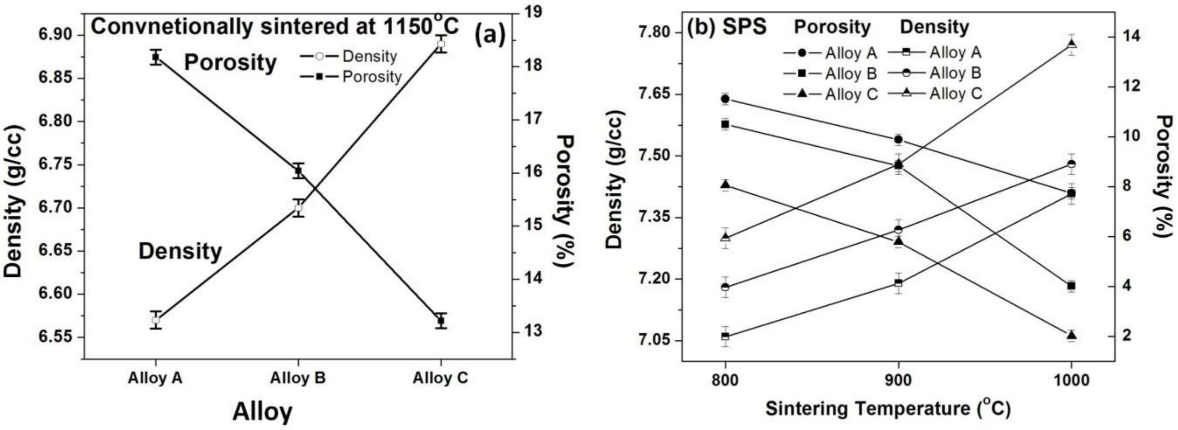

Fig.4.13: Variation of density and porosity values of (a) alloy A, alloy B and alloy C processed by conventional sintering at 1150°C, (b) alloys processed by spark plasma sintering at 800 °C, 900 °C, 1000 °C

Table.4.6: Density and porosity values of conventional and spark plasma sintered alloys

	Conventional sintering			Spark plasma sintering		
Alloy	Sintering temperature(°C)	Density (g/cc)	Porosity (%)	Sintering temperature(°C)	Density (g/cc)	Porosity (%)
Alloy A	1150	6.57	18.18	800	7.06	10.50
				900	7.19	8.841
				1000	7.40	7.743
Alloy B		6.70	16.04	800	7.18	11.52
				900	7.32	9.89
				1000	7.48	4.01
Alloy C		6.89	13.22	800	7.3	8.06
				900	7.48	5.79
				1000	7.77	2.02

Mechanical Properties

Fig.4.14 represents the apparent Vickers hardness values of all alloys sintered by conventional sintering and spark plasma sintering. It is observed that the hardness values of conventionally sintered alloys are in the range of 268 - 464 HV and the hardness values of samples sintered by SPS are in the range of 476 - 724 HV which records almost 1.5 to

2.0 times the hardness values of samples sintered by conventional method. This is due to presence of high porosity (Table 4.6) and substantial grain growth during sintering by conventional methods. On the other hand, the hardness values of alloys sintered by SPS show the function of sintering temperatures and it gradually increases with increasing sintering temperature as similar kind of trends were found in the previous section that the increase in density with increase in sintering temperature (Table 4.6). Hence, the highest hardness value obtained at 1000 °C samples for all the alloys. Furthermore, a close comparison of the densities achieved in different alloys concludes that the maximum hardness is obtained when processed by spark plasma sintering which yields the highest density too. The summary of the measured hardness values of all the alloys processed by both conventional and spark plasma sintering are shown in Table 4.7. From Table 4.7 it is also clear that the hardness is a function of alloy composition and alloy C offers highest hardness for both the processing routes.

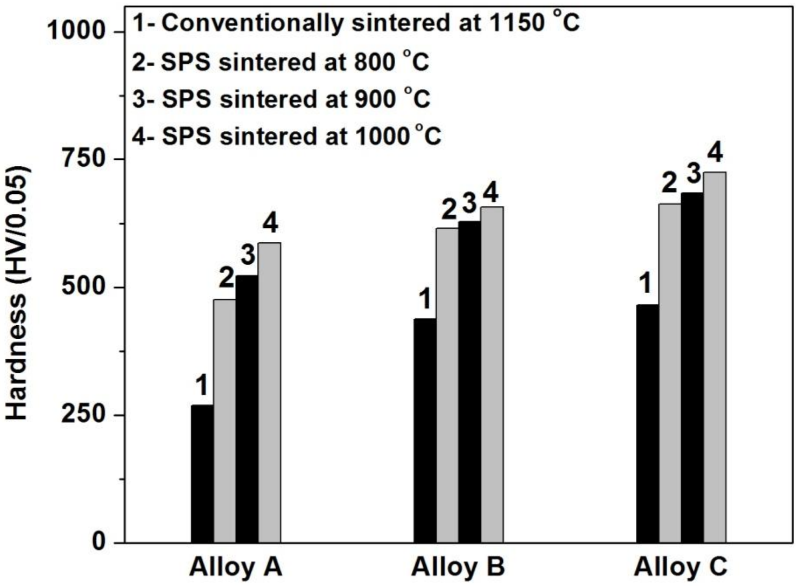

Fig.4.14: Vickers hardness values of all alloys processed by conventional sintering and spark plasma sintering (SPS)

The maximum hardness achieved is 724.9 HV, for alloy C spark plasma sintered at 1000 °C. In general it is taken into account that the apparent hardness depends on grain size, density, alloying elements and phase structure. Hence, apart from densification the nano-Y_2O_3 or nano-TiO_2 particles in alloy matrix of alloy B and alloy C respectively, contributed to their high hardness. Nano-oxide particles contribute significantly to mechanical properties of an alloy [23].

Wear Behaviour Study

In order to study the wear mechanism quantitatively, the volume loss of sample (*V*) at a given load has been calculated using the equation 4.3 recommended by ASTM standard *G* 99 – 95a.

$$\text{Disk volume loss(V)},\text{mm}^3 = \frac{\pi(r_1(w)^3)}{6(r_2)} \tag{4.3}$$

Where, r_1= wear track radius in mm, w = track width in mm, r_2= sphere radius in mm

It is valid to use this equation for present wear condition which follows the condition that there is no significant pin wear. Fig.4.16- 4.18 shows optical microscopy images of wear track surfaces, which are used to measure the wear track widths (w). From the calculated wear volume the wear rate is calculated using the equation 4.4. Fig.4.15 shows variation of wear rate per unit sliding distance ($\times 10^{-7}$ mm^3/mm), the wear rate was found to be high for samples sintered by conventional sintering than that of SPS samples.

$$\text{Wear rate} = \frac{V}{\text{total sliding distance}}, \text{mm}^3/\text{mm} \tag{4.4}$$

It was also observed that, in SPS alloys the wear rate decreases with increase in sintering temperature. The dependence of wear rate of the alloys on sintering route and sintering temperature is directly related to their respective density and hardness. In the previous section it was discussed that densities of samples sintered by conventional sintering are low compared to that of samples sintered by SPS. Therefore the wear rates obtained for all alloys consolidated by conventional sintering are in the range of 16.8×10^{-7} to 20.3×10^{-7} (mm^3/mm) while SPS alloys have comparatively very low wear rates of 3.17×10^{-7} to 8.87×10^{-7} (mm^3/mm). Also, the difference in wear resistance in terms of wear rate calculated is much less between the oxide dispersion strengthened alloys (ODS), alloy B and alloy C. But, the difference is significant between ODS (alloy B, alloy C) and non-ODS alloys (alloy A) clearly indicating the effect of nano-oxide dispersions on the material wear rate.

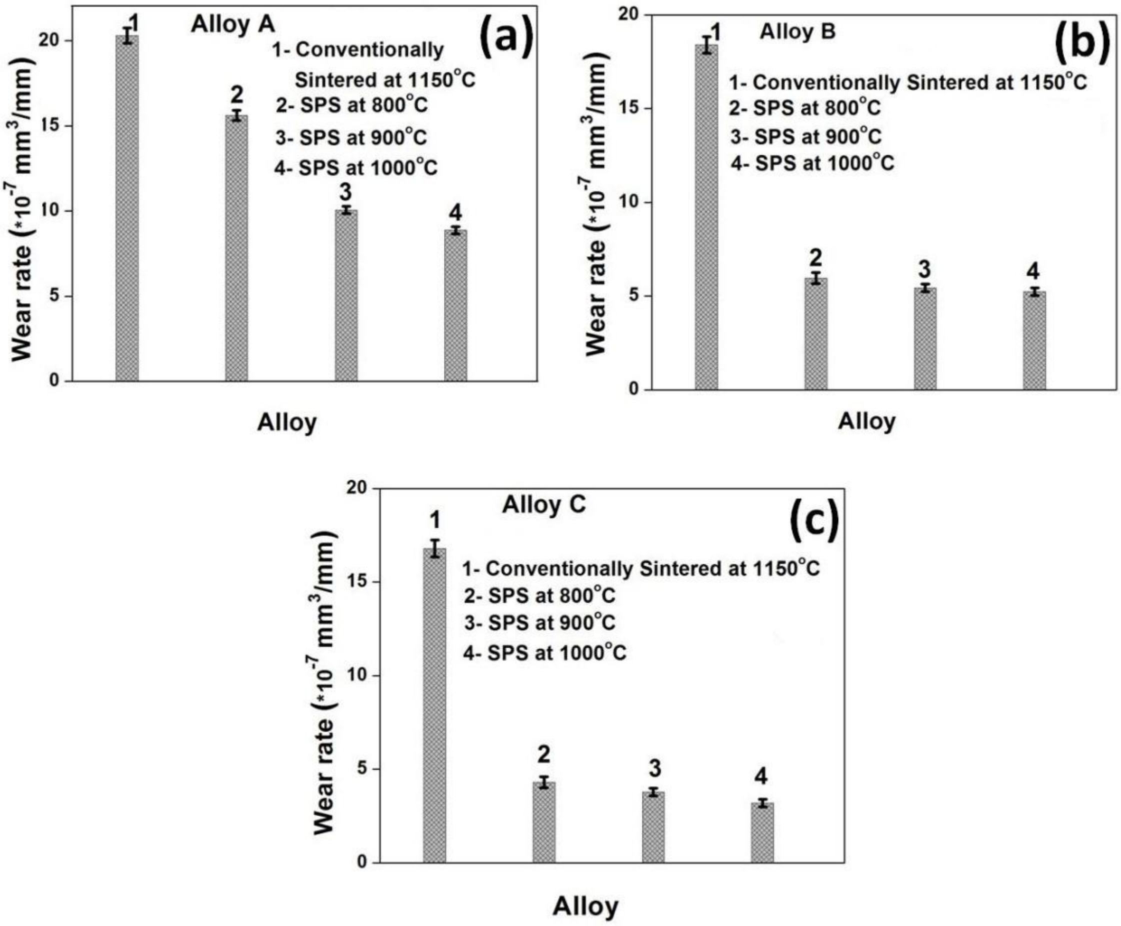

Fig.4.15: Wear rate values of all alloys processed by conventional sintering and spark plasma sintering

Material loss due to wear was significant in conventionally sintered alloys because of localised plastic deformation. As these sintered samples are of low density and more porous surface, wear happened very rapidly. In all the alloys both conventional and spark plasma sintered, SPS alloy C sintered at 1000 °C recorded the minimum wear rate of 3.17×10^{-7} (mm^3/mm). The higher wear resistance of this alloy is because of the presence of nano - TiO_2 particles which are harder than Y_2O_3 particles.

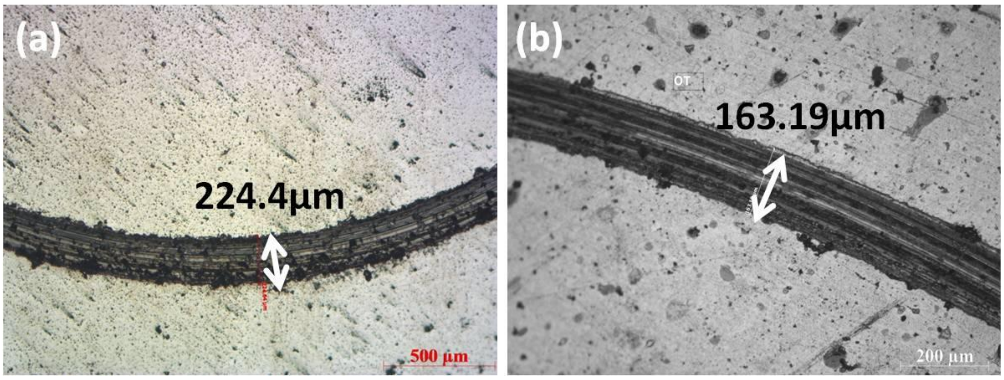

Fig.4.16: Optical microscope images showing wear tracks of (a) alloy A and (b) alloy B spark plasma sintered at 800 °C

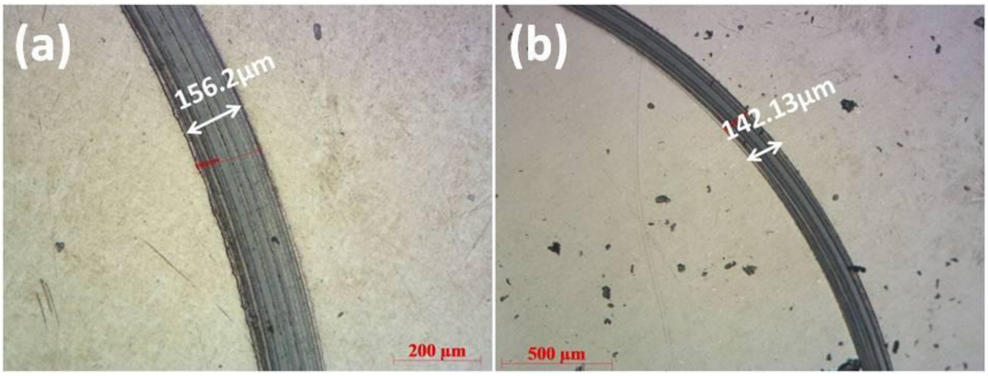

Fig.4.17: Optical microscope images showing wear tracks of (a) alloy B and (b) alloy C Spark plasma sintered at 900 °C

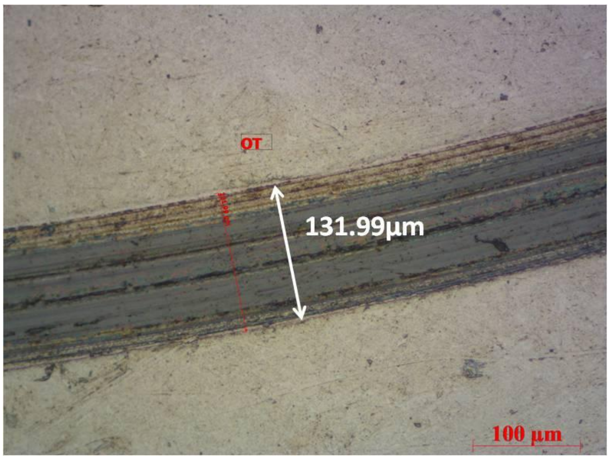

Fig.4.18: Optical microscope image showing wear track of alloy C spark plasma sintered at 1000 °C

4.3 Isothermal Oxidation Study of Consolidated Products

The studies on oxidation resistance under isothermal condition of all the alloys have been carried out in dry air at 1000 °C. Fig.4.19 shows the kinetics of isothermal oxidation in terms of cumulative weight gain (per unit area) as function of time (h). During the oxidation process it was observed that oxidation behaviour of spark plasma sintered alloys is better than that of conventionally sintered alloys. Better oxidation behaviour of SPS alloys is believed to be the result of their relatively fine microstructure and physical integrity. Fig.4.20 shows the rate constant of isothermal oxidation (K_p) during exposure to 1000 °C for SPS alloy A, alloy B, and alloy C (sintered at 900^{o}C) and conventionally sintered alloy A, alloy B, and alloy C. It may be noted from Fig.4.20 that the rate constant of alloy A is high and that of alloy C is low for both the sintering techniques. Conventionally sintered alloys have higher rate constant (K_p) of isothermal oxidation than that of SPS alloys and among which alloy C has lower rate constant value.

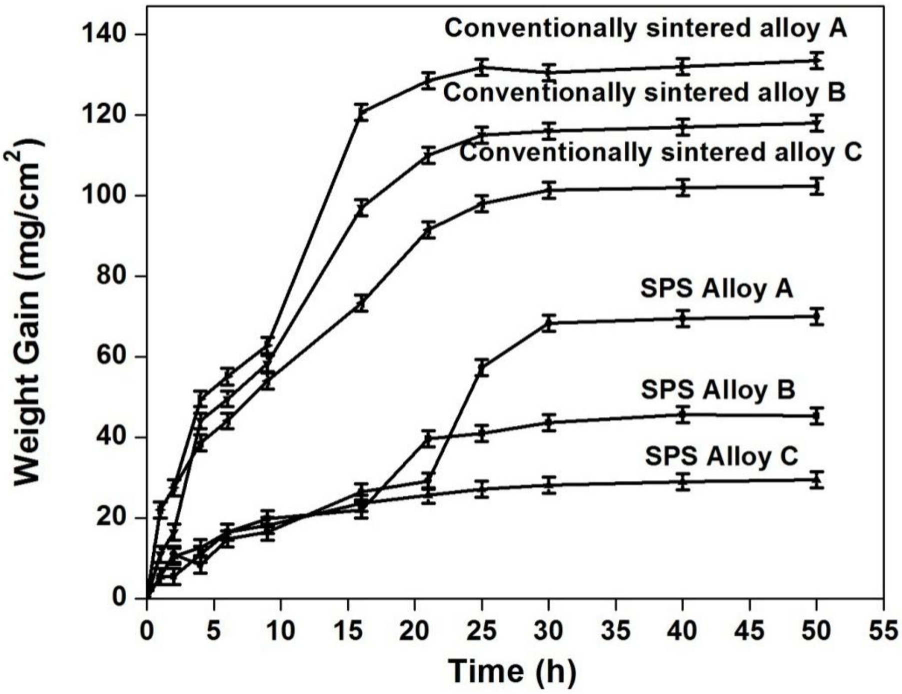

Fig.4.19: Kinetics of isothermal oxidation of SPS alloy A, alloy B and alloy C (sintered at 900 °C) and conventionally sintered alloy A, alloy B and alloy C in terms of mass gain per unit area as a function of time during isothermal exposure to 1000 °C in dry air

In all the alloys, the rate of weight gain is very quick in the initial stages and reaches a steady state beyond certain duration of time. The steady state is reached because of the formation of a protective layer on the sample surface. The parabolic law equation (equation 4.5) represents the kinetics of isothermal oxidation.

$$(\Delta W)^n = (K_p)(t) \tag{4.5}$$

Where, ΔW is mass gain per unit area (mg/cm^2), t is the time (h), n value is taken as 2, and K_p is the rate constant.

The material loss due to isothermal oxidation at 1000 °C is least for SPS alloy C. While in conventionally sintered alloy A it was found to be highest. The fine grain structure of SPS alloys had beneficial effect on their oxidation behaviour.

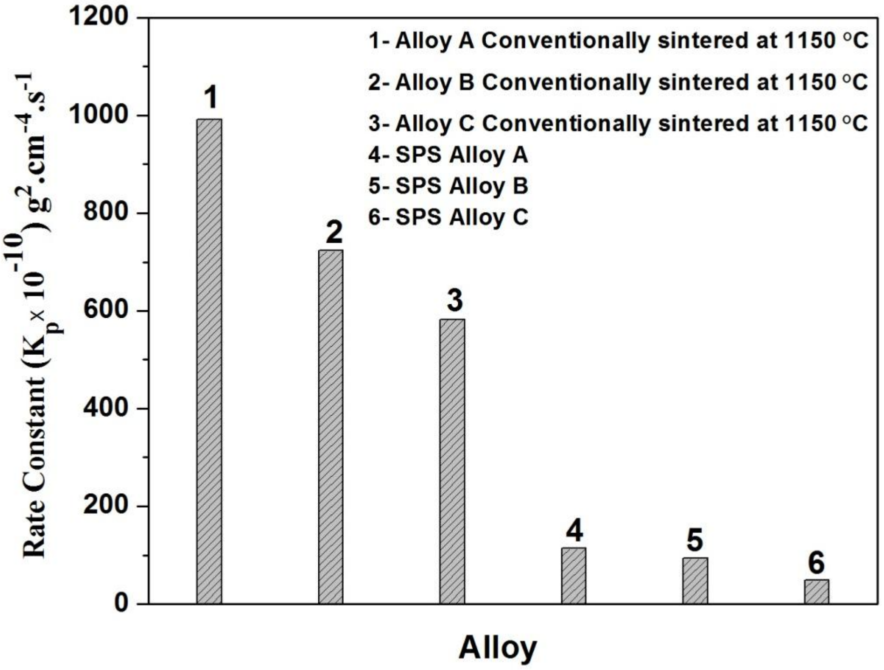

Fig.4.20: Rate constant during isothermal exposure to 1000 °C dry air for alloy A, alloy B and alloy C consolidated by two different processes namely; conventional sintering at 1150 °C and spark plasma sintering at 900 °C

Evidently from Fig.4.19 and Fig.4.20, depending on the alloy composition and sintering route, different oxidation behavior of alloys were observed, which are: 1. Growth of a thin protective oxide scale with small mass change, 2. Accelerated attack with spallation with significant material loss [68]. Fig.4.21 shows the microstructures of oxide scales on conventionally sintered and SPS samples. The surface was covered with a compact oxide scale consisting of small grains of less than 2 µm in size and big nodules of about 2-3 µm in size such that the small grains fill up the gaps among the bigger ones. Scale formation and growth in conventionally sintered alloy A was found to be greater than that of all other samples. Uniform protective oxide layer was observed on SPS alloy A, B and C which explains lowest weight gain of these alloys per unit time of exposure to 1000 °C temperature. In these alloys the formation of $(Fe, Cr)_2O_3$ inhibits faster diffusion of alloy elements because of nano-crystalline structure. This causes decrease in parabolic rate of oxidation compared to conventionally sintered alloys. Fig.4.21 (a) and Fig.4.2 (b) of conventionally sintered alloys show no indication of early oxide layer formation but their surfaces have saturated with increasing amounts of Fe and Cr oxides upon prolonged exposure to 1000 °C. In oxide dispersion strengthened steels Y_2O_3/TiO_2 segregates at the grain boundaries which may reduce the (Cr^{+3}/Fe^{+3}) cations moving outward across grain boundaries. This means that the oxide particles also reduce the inward oxygen flow.

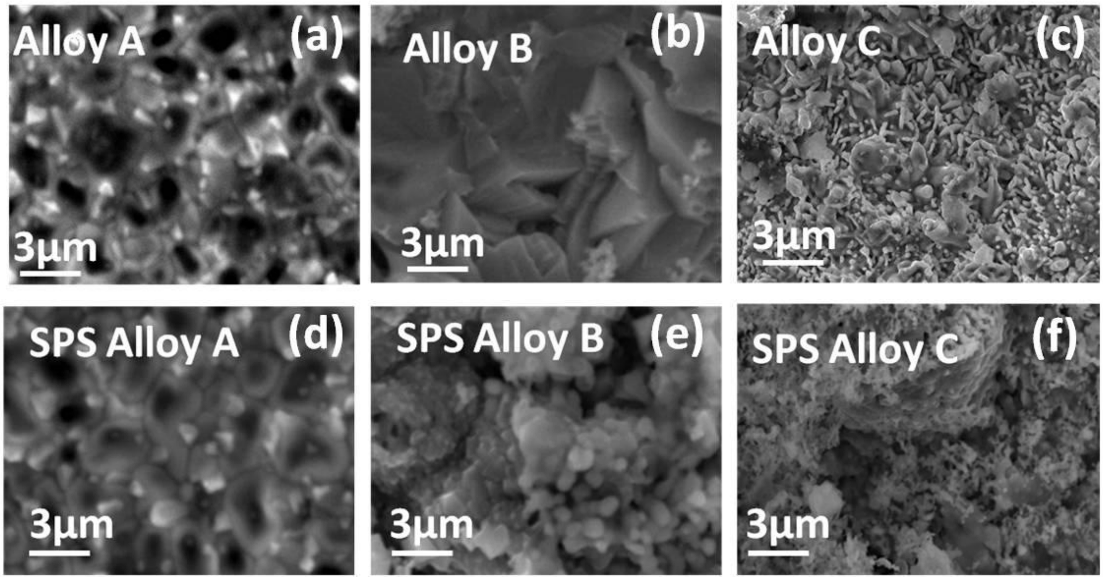

Fig.4.21: SEM micrographs of conventionally sintered (a) alloy A, (b) alloy B, and (c) alloy C, and spark plasma sintered (d) alloy A, and (e) alloy B and (f) alloy C after isothermal oxidation at 1000 °C for 50 h

From the detailed microstructural characterization of the oxide scale of all the alloys it is clear that the discontinuous Cr_2O_3 layer that formed at the beginning of oxidation, was not sufficient to protect the alloys from internal oxidation.However the mechanism in which oxidation occurs in metallic materials can be explained by grain boundary diffusion at the oxidation temperature. Previous investigations on oxidation behaviour [10] of metallic materials prove that when exposed to long durations at high temperature, these materials undergo grain coarsening through diffusion. This kind of diffusion follows equation 4.6 where in, D_e is total effective diffusion co-efficient of the grain, D_b is the grain boundary diffusion and D_v is the average volume diffusion of the grain and V_f is the volume fraction of grain boundaries in the polycrystalline materials. V_f = psx/*d*, where *p* is the numerical factor defending on grain shape, (*p* = 1 for parallel grain boundaries), *x* is the grain boundary thickness, *s* is the segregation factor and *d* is the spacing between grain boundary.

$$D_e = V_f D_b + (1 - V_f) D_v \tag{4.6}$$

While at grain boundaries of non-ODS microstructures, cation and oxygen flux would be greater resulting in higher oxidation and scale formation. The Fe_{+2} or Fe_{+3} ions migrate towards the free surface leading to the formation and rapid growth of Fe_2O_3. Blocked by Cr_2O_3, Fe_2O_3 nucleates and grows discontinuously in areas such as the non-compact Cr_2O_3 scale or micro-defective areas; leading to some bulges and pores. Subsequently, outward diffusion of Cr into Fe_2O_3 scale leads to dissolution of Cr_{3+} in Fe_2O_3 lattice to form $(Fe,Cr)_2O_3$ mixed oxide scale. This Cr diffusion and dissolution not only causes formation of stable $(Fe,Cr)_2O_3$ phase, it also fills the gaps within Cr_2O_3-rich scales in areas without Fe_2O_3 and hinders the inward diffusion of oxygen to restrict the formation or continuous growth of the oxide scale. The chemical reactions during oxidation can be summarized as follows:

$$4Cr + 3O_2 \rightarrow 2Cr_2O_3 \tag{4.7}$$

$$4Fe + 3O_2 \rightarrow 2Fe_2O_3 \tag{4.8}$$

$$2Cr + Fe_2O_3 \rightarrow (Fe, Cr)_2O_3 \tag{4.9}$$

X-ray diffraction analysis carried out on oxidised specimen gave an overview of the oxide phases on the specimen surface. Among all peaks, prominent were of Cr_2O_3 and Fe_2O_3phases and $(Fe, Cr)_2O_3$ phase was also identified. These are the most common oxides which exist in oxide film on austenitic stainless steel. XRD results of SPS alloys after oxidation for 50 h at 1000 °C shown in Fig.4.23 suggest the presence Cr_2O_3 in considerable amount.

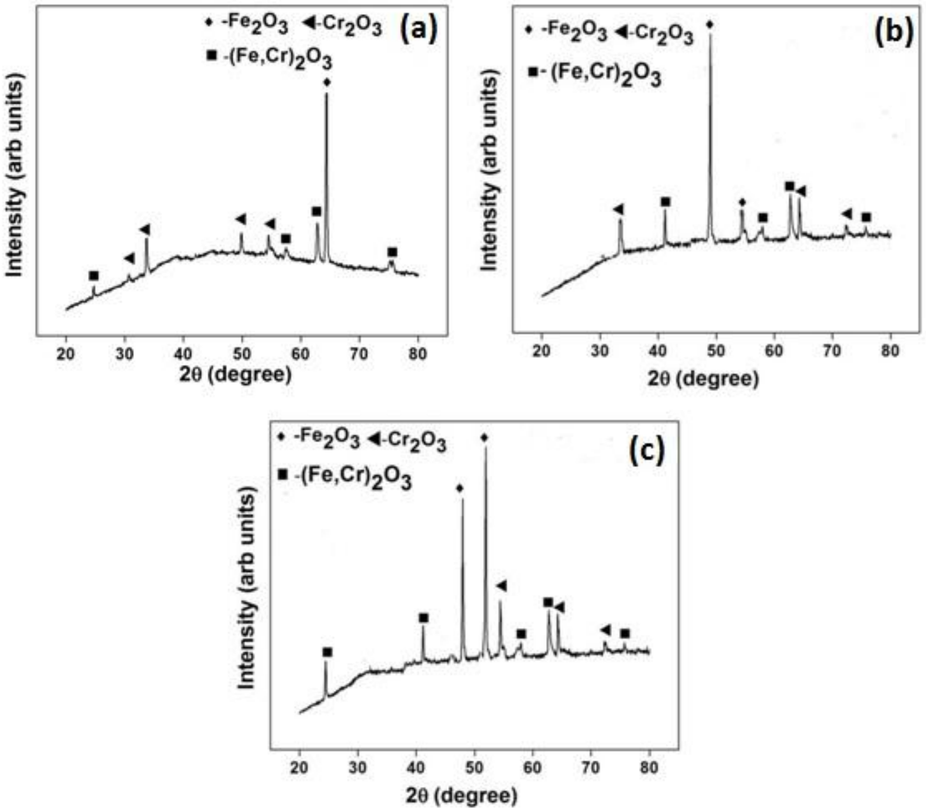

Fig.4.22: X-ray diffraction patterns of conventionally sintered (a) alloy B,(b) alloy C after isothermal oxidation at 1000 °C for 50 h

While Fe_2O_3 is the predominant phase in oxide layer of samples sintered by conventional sintering, shown in Fig.4.22. Cr_2O_3 is taken as the most protective oxide owing to very low diffusion constants for both metal ions and oxygen.

Therefore, with all these details combined it can be deduced that the present austenitic (with nano-oxide dispersed) SPS alloys have high oxidation resistance. The formation of $(Fe,Cr)_2O_3$ phase is because both Cr and Fe have same crystal structure (BCC), completely soluble in each other and hence forming a solid-solution of chromium iron oxides. The weight gain (mg/cm^2) per unit time results obtained, shown in Fig.4.19, reflects the minimal scale formed on SPS alloy surfaces. The rate constant of spark plasma sintered alloys increased with decreasing sintering temperature. Rate constant of conventionally sintered alloy A was found to be highest.

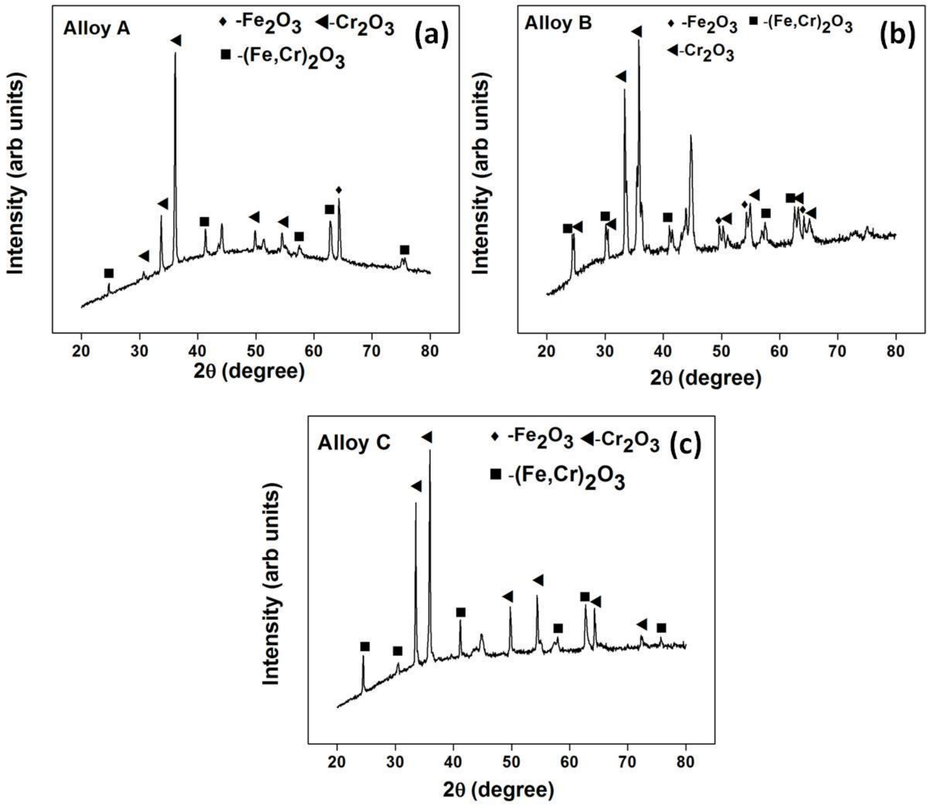

Fig.4.23: X-ray diffraction patterns of SPS (a) alloy A, (b) alloy B, and (c) alloy C after isothermal oxidation at 1000 °C for 50 h

4.4 Comparison of Properties

Density, porosity and physical integrity contribute towards mechanical behaviour of all the developed alloys and strongly depend upon alloy composition, sintering temperature and processing route. For SPS alloys, as sintering temperature increases from 800 °C – 1000 °C density increases and porosity decreases. Spark plasma sintered samples have better density (Table 4.7) compared to those produced by conventional sintering process.

This is because process parameters play a vital role in achieving highest level of densification. In spark plasma sintering rapid agglomeration of powder particles facilitates retaining of fine grain structure. While in conventional sintering, the 1 hour sintering time at 1150 °C was sufficient for diffusion and grain coarsening during the process. Absence of required pressure, for desired agglomeration, in this process leaves some of the pores from compaction without any change, resulting in low dense products.

As stated before, variation in hardness of sintered samples depends on sintering temperature, alloy composition, density and porosity and processing route. With all other process parameters maintained constant hardness of the sintered alloys increased with increase in sintering temperature. SPS alloy C sintered at 1000 °C has highest value of hardness while conventionally sintered alloy A has lowest hardness. The hardness value of alloy C is the highest as compared to other two alloys this because the presence of nano-TiO_2 particles which have higher elastic modulus (288 GPa) than that of nano-Y_2O_3 particles (173 GPa). This is also described from the chemical structure of TiO_2 which consists of two distorted tetrahedral site oxygen atoms (of four O atoms) in the unit cell of TiO_2 are responsible for the high hardness of TiO_2. In alloy A the absence of any particle reinforcement results in even lower hardness than alloy B. Since hardness of nano-particles directly affects the hardness of the sintered sample, alloy C has higher hardness than the other two alloys. The contribution of nano-TiO_2 particles in conventionally sintered alloy C is neutralized by its low density. But in SPS alloy C with above 95% density the same dispersion which has contributed to more refined microstructure enhanced the hardness.

Table 4.7: Summary of Physical and Mechanical Properties of all Alloys Developed by Conventional and Spark Plasma Sintering

	Alloy	Sintering temperature (°C)	Density (g/cc)	Porosity (%)	Hardness (HV)	Wear Rate ($\times 10^{-7}$ mm^3/mm)
Conventional Sintering	Alloy A	1150	6.57	18.18	268.0	20.30
	Alloy B		6.70	16.04	437.6	18.40
	Alloy C		6.89	13.22	464.9	16.80
Spark Plasma Sintering	Alloy A	800	7.06	10.50	476.0	15.62
		900	7.19	8.84	522.6	10.06
		1000	7.40	7.74	586.4	8.87
	Alloy B	800	7.18	11.52	615.0	5.95
		900	7.32	9.89	615.0	5.42
		1000	7.48	4.01	628.0	5.23
	Alloy C	800	7.30	8.06	657.0	4.30
		900	7.48	5.79	684.2	3.77
		1000	7.77	2.02	724.4	3.17

Wear resistance of the sintered alloys increased with increase in sintering temperature for both the consolidation processes as it happened for hardness. The wear tests conditions having maintained same for all alloys, the difference in their wear rates points out to dependence of wear behaviour on alloy composition, sintering route and sintering temperature. Higher wear resistant properties were obtained for SPS alloys compared to that of conventionally sintered alloys. However among SPS alloys, nano-TiO_2 dispersed alloy (alloy C), sintered at 1000 °C is better resistant to wear than the other alloys.

Oxidation resistance properties also depend on alloy composition, sintering temperature, sintering route and oxidation time. In conventionally sintered alloys presence of Fe_2O_3 phase (Fig.4.21) is identified to be more in the oxide scale which is the result of greater oxidation compared to that of SPS alloys. SPS Alloy C has superior oxidation resistance property than all other alloys. Due to fine grain structure the formation of Cr_2O_3happened much faster on SPS alloy surfaces and hence protecting the alloys. The XRD results of oxidised SPS samples indicate presence of Cr_2O_3 in higher amounts than Fe_2O_3.

Chapter 5

Summary and Conclusion

In the present study, a comprehensive effort has been made to develop austenitic alloys with compositions 70Fe-19.0Cr-11.0Ni (alloy A), 69.0Fe-19.0Cr-11.0Ni-1.0Y_2O_3 (alloy B) and69.0Fe-19Cr-11Ni-1.0TiO_2 (alloy C) (in wt. %) by mechanical alloying and subsequent consolidation by conventional sintering and spark plasma sintering. As mechanical alloying yields powders, a major effort in this work has been devoted to explore different routes of consolidation and optimizing relevant sintering parameters for developing bulk components retaining the novel microstructure obtained by mechanical alloying. By evaluating the results in terms of synthesis and characterization, consolidation, physical properties (density and porosity), mechanical properties (hardness and wear resistance property) and high temperature oxidation resistance in three sets of alloys with variation of alloy composition and sintering temperature a considerable volume of novel and new understanding about effect of nano-oxide dispersion and sintering temperature on the present austenitic stainless steel has emerged. Major outcome of the present study are summarized as follows:

1. Mechanical alloying is a potential route for synthesis of nano- Y_2O_3/TiO_2 dispersed austenitic stainless steel powders with nominal compositions of 70.0Fe-19.0Cr-11.0Ni (alloy A), 69.0Fe-19.0Cr-11.0Ni-1.0Y_2O_3 (alloy B) and 69.Fe-19 Cr-11 Ni-1.0TiO_2 (alloy C).

2. From the XRD analysis it is found that alloy powders at different stages (1 h, 5 h, 10 h, 20 h, 30 h and 40 h) during mechanical alloying indicates the presence of predominant phase austenite (FCC) with also evolution of ferrite (BCC) phase after 1 h of milling.

3. There was gradual reduction in crystallite size with increase of milling time. The crystallite size reduction from 450 to 11.73 nm for alloy A, 459 to 9.51 nm for alloy B and 416 to 7 nm for alloy C respectively, with increase in milling time.

4. Particle size analysis at different times (0 h, 5 h, 10 h, 20 h, 30 h and 40 h) of ball milling of alloy A powder show reduction in particle size from 51 to 3.5 μm. Similar

kind of trend has been observed through SEM analysis that the average particle size reduced from 40 to 3.4 µm.

5. Phase evolution of consolidated products (conventional sintered and SPS alloys) by XRD analysis showed presence of predominant austenite and ferrite phases for all alloys. XRD analysis of alloy Cshowed presence of intermetallic precipitate phase Ni_3Ti along with the presence of austenite and ferrite phases.

6. Bulk mechanical (hardness, wear resistance) properties of present alloys consolidated by spark plasma sintering (SPS) record high levels of hardness (476–724.4 HV) which is 1.5 to 2.0 times higher than that of conventionally sintered alloys (268-464 HV).Alloy C sintered by sample spark plasma sintered at 1000 °C records superior hardness (724.4 HV) compared to other alloy samples. Similar kind of trend was observed for its wear study. It is observed that alloy C has least wear rate of 3.17×10^{-7} mm^3/mm.

7. The oxidation resistance property of oxide dispersion strengthened alloys (alloy B and alloy C) has improved significantly compared to alloy A. The rate of oxidation decreased with increase in sintering temperature in SPS alloys and is least for alloy C spark plasma sintered at 1000 °C.

8. Also, it is clear from isothermal oxidation study that the samples which are consolidated by spark plasma sintering form a protective oxide scale much faster than conventionally sintered samples and hence restricting oxidation only to surface of the sample. The improvement in oxidation resistance property in SPS alloy C is attributed to the formation of a relatively continuous oxides of Fe and Cr with the following compositions: Fe_2O_3, $Cr_2O_3$and $(Fe,Cr)_2O_3$, presence of which was confirmed by X-ray diffraction analysis.

Thus, the above mentioned conclusions suggest that mechanical alloying followed by spark plasma sintering is a promising route for synthesizing austenitic stainless steel with nano-oxide dispersed matrix offering attractive mechanical and oxidation resistance properties. And that the nano-oxide dispersions significantly improve overall properties of the present austenitic stainless steel.

Future Work

- The factors which control the mechanical properties of the present oxide dispersion strengthened (ODS) alloys i.e. hardness of nano-particles, size and distribution of nano-particles in the matrix, porosity volume fraction in the alloys, and grain size could be further studied in detail.

- The effect of different nano-particles reinforcement on the wear resistance, i.e. the effect of abrasive mechanism after ploughing through the nano-particle could be investigated for better understanding of enhanced wear resistance property of oxide dispersion strengthened (ODS) alloys.

Bibliography

[1] Q. Zhang, Y. Zheng, X. Su, K. Yin, X. Tang, and C. Uher.Enhanced power factor of $Mg_2Si_{0.3}Sn_{0.7}$ synthesized by a non-equilibrium rapid solidification method. *Scripta Materialia*, 96: 1 -- 4, November 2015.

[2] C. Suryanarayana, Mechanical alloying and milling.*Progress in Materials Science*. 46(1-2):1-- 184, January 2001.

[3] J. S. Benjamin, Mechanical alloying - A perspective.*Metal Powder Report*. 45(2):122 -- 127, February 1990.

[4] I. Hilger, M. Tegel, M. J. Gorley, P. S. Grant, T. Weißgärber, and B. Kieback.The structural changes of Y_2O_3 in ferritic ODS alloys during milling.*Journal of Nuclear Materials*,447(1):242 -- 247, January 2014.

[5] Q. X. Sun, Q. F. Fang, Y. Zhou, Y. P. Xia, T. Zhang, X. P. Wang, and C. S. Liu. Development of oxide dispersion strengthened ferritic steel prepared by chemical reduction and mechanical milling.*Journal of Nuclear Materials*, 439(1-3):103--107, April 2013.

[6] Q. X. Sun, T. Zhang, X. P. Wang, Q. F. Fang, T. Hao, and C. S. Liu. Microstructure and mechanical properties of oxide dispersion strengthened ferritic steel prepared by a novel route.*Journal of Nuclear Materials*, 424(1-3):279 -- 284, January 2012.

[7] K. H. Lo, C. H. Shek, and J. K. L. Lai.Recent developments in stainless steels. *Materials Science and Engineering R*, 65(4-6):39 -- 104, April 2009.

[8] Y. Hosoi, Introduction to stainless steel. *Journal of Japan Institute of Light Metals.*37(9):624 -- 635, 1987.

[9] B. J. Marques, C. M. Fernandes, and a. M. R. Senos. Sintering, microstructure and properties of WC-AISI304 powder composites.*Journal of Alloys and Compounds*,562:164 -- 170, February 2013.

[10] M. Fulger, M. Mihalache, D. Ohai, S. Fulger, and S. C. Valeca.Analyses of oxide films grown on AISI 304L stainless steel and Incoloy 800HT exposed to supercritical water environment.*Journal of Nuclear Materials*, 415(2):147 -- 157, May 2011.

[11] J. Capus. Raising strength in PM austenitic stainless steels.*Metal Powder Report* . 66(1):25 -- 27, February 2011.

[12] O. Ertugrul, H.-S. Park, K. Onel, and M. Willert-Porada. Effect of particle size and heating rate in microwave sintering of 316L stainless steel.*Powder Technology*.253:703 -- 709, January 2014.

[13] D. Oleszak, A. Grabias, M. Pękała, A. Świderska-Środa, and T. Kulik. Evolution of structure in austenitic steel powders during ball milling and subsequent sintering. *Journal of Alloys and Compounds*. 434–435:340 -- 343, 2007.

[14] J. Liu, G. Li, B. Peng, and X. Zhang. Effect of Nitrogen on Structure and Properties of Ultra-Fine Austenitic Stainless Steel.*Journal of Iron and Steel Research, International*,14(5):310 -- 315, September 2007.

[15] R. L. Klueh, J. P. Shingledecker, R. W. Swindeman, and D. T. Hoelzer. Oxide dispersion-strengthened steels: A comparison of some commercial and experimental alloys.*Journal of Nuclear Materials*, 341(2–3):103 -- 114, January 2005.

[16] S. K. Karak, J. Dutta Majumdar, Z. Witczak, W. Lojkowski, and I. Manna. Microstructure and mechanical properties of nano-Y_2O_3 dispersed ferritic alloys synthesized by mechanical alloying and consolidated by hydrostatic extrusion.*Materials Science and Engineering: A*, 580:231 -- 241, May 2013.

[17] F. Liu, Y. Liu, Y. Wen, Y. Dou, D. Zhao, and C. T. Liu. Microstructures and mechanical properties of Fe–14Cr–3W–Ti–Y_2O_3 steel with 1wt.% Cu addition fabricated by a new method. *Journal of Nuclear Materials*, 414(3):422 -- 425, May 2011.

[18] R. Kasada, N. Toda, K. Yutani, H. S. Cho, H. Kishimoto, and a. Kimura, “Pre- and post-deformation microstructures of oxide dispersion strengthened ferritic steels,” *Journal of Nuclear Materials*, 367 -- 370: 222 -- 228, August 2007.

[19] S. Pasebani and I. Charit. Effect of alloying elements on the microstructure and mechanical properties of nanostructured ferritic steels produced by spark plasma sintering.*Journal of Alloys and Compounds*, 599:206 -- 211, February 2014.

[20] M. J. Alinger, G. R. Odette, and D. T. Hoelzer. On the role of alloy composition and processing parameters in nanocluster formation and dispersion strengthening in nanostuctured ferritic alloys.*Acta Materialia*, 57(2):392 -- 406, October 2008.

[21] H. Oka, M. Watanabe, N. Hashimoto, S. Ohnuki, S. Yamashita, and S. Ohtsuka. Morphology of oxide particles in ODS austenitic stainless steel.*Journal of Nuclear Materials*, 442(1-3 SUPPL.1):164 -- 168, May 2013.

[22] Y. Xu, Z. Zhou, M. Li, and P. He. Fabrication and characterization of ODS austenitic steels. *Journal of Nuclear Materials*, 417(1-3):283 -- 285, 2011.

[23] P. Susila, D. Sturm, M. Heilmaier, B. S. Murty, and V. Subramanya Sarma. Microstructural studies on nanocrystalline oxide dispersion strengthened austenitic (Fe–18Cr–8Ni–2W–0.25Y_2O_3) alloy synthesized by high energy ball milling and vacuum hot pressing.*Journal of Materials Science*, 45(17):4858 -- 4865, February 2010.

[24] M. Wang, Z. Zhou, H. Sun, H. Hu, and S. Li. Microstructural observation and tensile properties of ODS-304 austenitic steel.*Materials Science and Engineering A*,559:287 -- 292, 2013.

[25] S. K. Karak, C. S. Vishnu, Z. Witczak, W. Lojkowski, J. Dutta Majumdar, and I. Manna. Studies on wear behavior of nano-Y_2O_3 dispersed ferritic steel developed by mechanical alloying and hot isostatic pressing.*Wear*, 270(1-2):5 -- 11, October 2010.

[26] M. Broseghini, L. Gelisio, M. D’Incau, C. L. Azanza Ricardo, N. M. Pugno, and P. Scardi. Modeling of the planetary ball-milling process: The case study of ceramic powders.*Journal of the European Ceramic Society*, September 2015.

[27] Y.S. Kwon, K. B. Gerasimov, and S.-K. Yoon. Ball temperatures during mechanical alloying in planetary mills.*Journal of Alloys and Compounds*, 346(1-2):276 -- 281, April 2002.

[28] A. Yazdani and A. Zakeri. An insight into formation of nanostructured coatings on metallic substrates by planetary ball milling.*Powder Technology*, 278:196 -- 203, March 2015.

[29] S. M. Hong, J. J. Park, E. K. Park, K. Y. Kim, J. G. Lee, M. K. Lee, C. K. Rhee, and J. K. Lee. Fabrication of titanium carbide nano-powders by a very high speed planetary ball milling with a help of process control agents.*Powder Technology*. 274:393 -- 401, 2015.

[30] Y. Kilinç, S. Öztürk, B. Öztürk, and I. Uslan. Investigation of milling characteristics of alumina powders milled with a newly designed vibratory horizontal attritor.*Powder Technology*, 146(3):200 -- 205, July 2004.

[31] R. Shashanka, and D. Chaira. Development of nano-structured duplex and ferritic stainless steels by pulverisette planetary milling followed by pressureless sintering. *Materials Characterization*,99:220 -- 229, 2015.

[32] C. Suryanarayana and N. Al-Aqeeli. Mechanically alloyed nanocomposites.*Progress in Materials Science*, 58(4):383 -- 502, 2012.

[33] L. Lü and M. O. Lai. *Mechanical Alloying*.2013.

[34] Z. Zhang, G. Yao, X. Zhang, J. Ma, and H. Lin. Synthesis and characterization of nickel ferrite nanoparticles via planetary ball milling assisted solid-state reaction.*Ceramics International*, 41(3):4523 -- 530, December 2014.

[35] C. Suryanarayana, E. Ivanov, and V. Boldyrev. The science and technology of mechanical alloying.*Materials Science and Engineering A*, 304–306:151 -- 158, 2001.

[36] J. S. Benjamin and T. E. Volin. The mechanism of mechanical alloying.*Metallurgical Tranactions*, 5(8):1929 -- 1934, August 1974.

[37] N. Oono, Q. X. Tang, and S. Ukai. Oxide particle refinement in Ni-based ODS alloy.*Materials Science and Engineering A*, 649:250 -- 253, 2016.

[38] C. L. Chen and Y. M. Dong. Effect of mechanical alloying and consolidation process on microstructure and hardness of nanostructured Fe-Cr-Al ODS alloys. *Materials Science and Engineering A*, 528(29-30):8374 -- 8380, August 2011.

[39] M. Zhao, Z. Zhou, J. Tan, Q. Ding, and M. Zhong. Effects of ball milling parameters on microstructural evolution and mechanical properties of W-3% Y composites.*Journal of Nuclear Materials*, 465:6 -- 12, June 2015.

[40] M. Nagini, R. Vijay, M. Ramakrishna, A. V. Reddy, and G. Sundararajan. Influence of the duration of high energy ball milling on the microstructure and mechanical properties of a 9Cr oxide dispersion strengthened ferritic–martensitic steel.*Materials Science and Engineering A*, 620:490 -- 499, 2015.

[41] P. Kuziora, M. Wyszyńska, M. Polanski, and J. Bystrzycki. Why the ball to powder ratio (BPR) is insufficient for describing the mechanical ball milling process. *International Journal of Hydrogen Energy*, 39(18):9883 -- 9887, April 2014.

[42] S. S. Razavi Tousi, R. Yazdani Rad, E. Salahi, I. Mobasherpour, and M. Razavi. Production of Al-20 wt.% Al_2O_3 composite powder using high energy milling," *Powder Technology*, 192(3):346 -- 351, February 2009.

[43] R. M. German. History of sintering: empirical phase.*Powder Metalurgy.*, 56(2):117 -- 123, 2013.

[44] G. D. Cremer. Powder Metallurgy. United States Patent. August 1944.

[45] G. F. Taylor. Apparatus for Making Hard Metal Compositions,United States Patent. February 1933.

[46] H. Cheng, D. Liu, H. Tang, S. Zhang, X. Ran, And H. Wang. Effect of Hot Isostatic Pressing on Fatigue Properties of Laser Melting Deposited AerMet100 Steel.*Journal of Iron and Steel Research International.*, 20(11):79 -- 84, 2013.

[47] L. Xu, R. Guo, C. Bai, J. Lei, and R. Yang. Effect of Hot Isostatic Pressing Conditions and Cooling Rate on Microstructure and Properties of Ti–6Al–4V Alloy from Atomized Powder.*Journal of Materials Science and Technology*,30(12):1289 -- 1295, May 2014.

[48] L. Chang, W. Sun, Y. Cui, F. Zhang, and R. Yang. Effect of heat treatment on microstructure and mechanical properties of the hot-isostatic-pressed Inconel 718 powder compact. *Journal of Alloys and Compounds*, 590:227 -- 232, February 2014.

[49] P. Yadoji, R. Peelamedu, D. Agrawal, and R. Roy. Microwave sintering of Ni-Zn ferrites: Comparison with conventional sintering. Materials Science and Engineering B: Solid-State Materials for Advanced Technology, 98(3):269 -- 278, February 2003.

[50] D. E. Clark, D. C. Folz, and J. K. West. Processing materials with microwave energy.*Materials Science and Engineering A*, 287(2):153 -- 158, 2000.

[51] C. Leonelli, P. Veronesi, L. Denti, A. Gatto, and L. Iuliano. Microwave assisted sintering of green metal parts.*Journal of Materials Processing and Technology*, 205(1–3):489 -- 496, 2008.

[52] R. R. Menezes, P. M. Souto, and R. H. G. a Kiminami. Microwave hybrid fast sintering of porcelain bodies.*Journal of Materials Processing and Technology*, 190(1-3):223 -- 229, February 2007.

[53] A. Michalski and K. Cymerman. Ni_3Al/diamond composites produced by pulse plasma sintering (PPS) with the participation of the SHS reaction.*Journal of Alloys and Compounds*, 636:196 -- 201, March 2015.

[54] M. Dias, F. Guerreiro, J. B. Correia, A. Galatanu, M. Rosiński, M. A. Monge, A. Munoz, E. Alves, and P. A. Carvalho. Consolidation of W–Ta composites: Hot isostatic pressing and spark and pulse plasma sintering.*Fusion Engineering and Design*, 99:1950 -- 1955, July 2015.

[55] A. M. Abyzov, M. J. Kruszewski, Ł. Ciupiński, M. Mazurkiewicz, A. Michalski, and K. J. Kurzydłowski. Diamond–tungsten based coating–copper composites with high thermal conductivity produced by Pulse Plasma Sintering.*Materials Design*, 76:97 -- 109, 2015.

[56] A. H. Pakseresht, A. H. Javadi, M. Bahrami, F. Khodabakhshi, and A. Simchi. Spark plasma sintering of a multilayer thermal barrier coating on Inconel 738 superalloy: Microstructural development and hot corrosion behavior.*Ceramic International,*pages 1–10, November 2015.

[57] M. Tokita. Mechanism of Spark Plasma Sintering. *Proceeding of NEDO International Symposium on Functionally Graded Materials*, pages 1–13, 1999.

[58] I. Sulima, P. Putyra, P. Hyjek, and T. Tokarski. Effect of SPS parameters on densification and properties of steel matrix composites.*Advanced Powder Technology*, 26(4):1152 -- 1161, June 2015.

[59] K. Rajan, V. S. Sarma, T. R. G. Kutty, and B. S. Murty. Hot hardness behaviour of ultrafine grained ferritic oxide dispersion strengthened alloys prepared by mechanical alloying and spark plasma sintering.*Materials Science Engineering A*, 558:492 -- 496, August 2012.

[60] C. Menapace, I. Lonardelli, M. Tait, and A. Molinari. Nanostructured/ultrafine multiphase steel with enhanced ductility obtained by mechanical alloying and spark plasma sintering of powders.*Materials Science Engineering A*, 517(1-2):1–7, March 2009.

[61] J. H. Schneibel, M. Heilmaier, W. Blum, G. Hasemann, and T. Shanmugasundaram. Temperature dependence of the strength of fine- and ultrafine-grained materials.*Acta Materialia*, 59(3):1300 -- 1308, 2011.

[62] V. C. Nardone and J. K. Tien. Pinning of Dislocations on the Departure Side of Strengthening Dispersoids. *Scripta Metallurgica*, 17:467 -- 470, 1983.

[63] H. Abe, S. M. Hong, and Y. Watanabe. Oxidation behavior of austenitic stainless steels as fuel cladding candidate materials for SCWR in superheated steam.*Nuclear Engineering and Design*, 280:652 -- 660, August 2014.

[64] M. Nezakat, H. Akhiani, S. Penttilä, S. Morteza, and J. Szpunar. Effect of thermo-mechanical processing on oxidation of austenitic stainless steel 316L in supercritical water.*Corrosion Science*, 94:197 -- 206, February 2015.

[65] E. J. Mittemeijer and U. Welzel. The ‘state of the art’ of the diffraction analysis of crystallite size and lattice strain. 223:552 -- 560, July 2008.

[66] R. Shashanka and D. Chaira. Optimization of milling parameters for the synthesis of nano-structured duplex and ferritic stainless steel powders by high energy planetary milling.*Powder Technology*, 278:35 -- 45, March 2015.

[67] K. N. Allahar, J. Burns, B. Jaques, Y. Q. Wu, I. Charit, J. Cole, and D. P. Butt. Ferritic oxide dispersion strengthened alloys by spark plasma sintering. *Journal of Nuclear Materials*, 443(1–3):256 -- 265, July 2013.

[68] R. Peraldi and B. A. Pint. Effect of Cr and Ni Contents on the Oxidation Behavior of Ferritic and Austenitic Model Alloys in Air with Water Vapor. *Oxidation of Metals*, 61(5–6):463 -- 483, 2004.

[69] P. Baláž, M. Achimovičová, M. Baláž, P. Billik, Z. Cherkezova-Zheleva, J. M. Criado, F. Delogu, E. Dutková, E. Gaffet, F. J. Gotor, R. Kumar, I. Mitov, T. Rojac, M. Senna, A. Streletskii, and K. Wieczorek-Ciurowa. Hallmarks of mechanochemistry: from nanoparticles to technology. *Chemical Society Review*, 42(18):7571–7637, 2013.

[70] H. Ates and E. Bahceci. Nano Malzemeler için Ü retim Y öntemleri. *Gazi University Journal of Science*, 3(2):483–499, 2015.

[71] G. S. Upadhyaya. Powder Metallurgy Technology. *Cambridge International Science Publishing*, August 2012.

[72] J. R. Blackford, G. Skouvaklis, M. Purser, and V. Koutsos. Friction on ice: stick and slip. *The Royal Society of Chemistry*, 156: 243-254, 2012.

Publications and Conference Presentations

1. Presented a paper on “Development of nano-oxide dispersed austenitic steels by mechanical alloying and conventional sintering”, NMD-ATM 2014, Nov 12th-15th, Pune.
2. Sravan Kumar Sambaraj, Swapan Kumar Karak, Sandeep ES, S.B. Chandrashekar “Development of nano-oxide dispersed 304L steels by mechanical milling and conventional sintering” , Materials Research (Accepted 26-Nov-2015).

Bio Data

Name	Sravan Kumar Sambaraj
Date of Birth	17-01-1991
Permanent Address	**7**-2-1768, Flat No.103, Classic Avenue Street no.4, Czech colony, Sanath Nagar Hyderabad Telangana- 500018
Email Id	sravan.sambaraj@gmail.com
Languages Known	Telugu, Hindi, and English

Educational Profile

Course	**Institution**	**Board/University**	**Year of Completion**	**Aggregate percentage of marks**
B.Tech	Mahatma Gandhi Institute of Technology, Hyderabad.	Jawaharlal Nehru Technological University, Hyderabad.	2012	68.7
12th Standard	Narayana Junior College, Hyderabad	Board of intermediate Education	2008	88.0
10th Standard	Johnson Grammar High School, Hyderabad.	SSC	2006	80.6